JGR Solid Earth

RESEARCH ARTICLE
10.1029/2021JB022548

Influence of Deformation and Fluids on Ti Exchange in Natural Quartz

Michel Bestmann[1], Giorgio Pennacchioni[2], Bernhard Grasemann[3], Benjamin Huet[4], Michael W. M. Jones[5], and Cameron M. Kewish[6,7]

[1]GeoZentrum Nordbayern, Department of Geography and Geosciences, Friedrich-Alexander-University Erlangen-Nürnberg (FAU), Erlangen, Germany, [2]Department of Geosciences, University of Padova, Padova, Italy, [3]Department of Geology, University of Vienna, Vienna, Austria, [4]Department of Hard Rock Geology, Geological Survey of Austria, Vienna, Austria, [5]Central Analytical Research Facility, Queensland University of Technology, Brisbane, QLD, Australia, [6]Australian Synchrotron, Clayton, VIC, Australia, [7]Department of Chemistry and Physics, School of Molecular Sciences, La Trobe University, Melbourne, VIC, Australia

Key Points:

- Ti-in-quartz re-equilibration is possible during subgrain rotation recrystallization even at lower greenschist facies conditions
- Ti resetting depends on the availability of aqueous fluids along interconnected grain boundaries, independently of the accumulated strain
- Partial Ti resetting also takes place along dry subgrain boundaries

Supporting Information:

Supporting Information may be found in the online version of this article.

Correspondence to:

M. Bestmann,
michel.bestmann@fau.de

Citation:

Bestmann, M., Pennacchioni, G., Grasemann, B., Huet, B., Jones, M. W. M., & Kewish, C. M. (2021). Influence of deformation and fluids on Ti exchange in natural quartz. *Journal of Geophysical Research: Solid Earth*, *126*, e2021JB022548. https://doi.org/10.1029/2021JB022548

Received 10 JUN 2021
Accepted 14 NOV 2021

Author Contributions:

Conceptualization: Michel Bestmann, Giorgio Pennacchioni, Bernhard Grasemann
Data curation: Michel Bestmann
Formal analysis: Michel Bestmann
Funding acquisition: Michel Bestmann
Investigation: Michel Bestmann, Giorgio Pennacchioni, Bernhard Grasemann
Methodology: Michel Bestmann, Benjamin Huet, Michael W. M. Jones, Cameron M. Kewish
Project Administration: Michel Bestmann
Resources: Michel Bestmann

Abstract Using a combination of microstructural, spectroscopic, and geochemical analyses, we investigate how subgrain rotation recrystallization and fluid migration affect Ti concentration [Ti] in naturally deformed quartz veins from the Prijakt Nappe (Austroalpine Unit, Eastern Alps). These coarse-grained quartz veins, that formed at amphibolite facies conditions, were overprinted by lower greenschist facies deformation to different degrees. During the overprint, subgrain rotation recrystallization was dominant during progressive deformation to ultramylonitic stages. The initial [Ti] (3.0–4.7 ppm) and cathodoluminescence (CL) signature of the vein crystals decrease during deformation mainly depending on the availability of fluids across the microstructure. The amount of strain played a subordinate role in resetting to lower [Ti] and corresponding darker CL shades. Using a microstructurally controlled analysis we find that the most complete re-equilibration in recrystallized aggregates ([Ti] of 0.2–0.6 p.m.) occurred (a) in strain shadows around quartz porphyroclasts, acting as fluid sinks, and (b) in localized microshear zones that channelized fluid percolation. [Ti] resetting is mainly observed along wetted high angle boundaries (misorientation angle >10–15°), with partial [Ti] resetting observed along dry low angle boundaries (<10–15°). This study shows for the first time that pure subgrain rotation recrystallization in combination with dissolution-precipitation under retrograde condition provide microstructural domains suitable for the application of titanium-in-quartz geothermobarometry at deformation temperatures down to 300–350°C.

Plain Language Summary For over 10 years, the TitaniQ geothermometer has been used to constrain deformation temperatures in quartz-rich rocks. The calibration of the thermometer rests on the direct correlation of the titanium trace element concentration in quartz with respect to the ambient temperature. However, the processes and parameters which lead to re-equilibration of the Ti-in-quartz system during deformation are not yet fully understood. Here we analysed deformed quartz veins from the Eastern Alps applying a combination of microstructural, spectroscopic, and geochemical analyses. In contrast to recent studies which highlight the importance of stain, we show that the availability of free grain boundaries, fluids, and their partitioning play the dominant role in Ti resetting toward lower concentrations in our studied case of retrograde deformation. We employ a robust analytical approach to investigate the interplay between grain-scale deformation, fluid-rock interactions, and geochemical exchange during increasing strain in the quartz mylonites. With this approach, the microstructures representing most re-equilibrated sites for the application of the titanium-in-quartz geothermometer can be readily identified, even at lower greenschist facies deformation conditions and a recrystallization regime dominated by subgrain rotation.

1. Introduction

Deformation in the Earth's crust is commonly accommodated in quartz-rich rocks. Especially pure quartz veins localize a final increment of strain under retrograde deformation (e.g., Ceccato et al., 2017; Trepmann & Seybold, 2019). Therefore, estimating the temperature of quartz deformation is crucial to unravel the deformation history and provides an important contribution with respect to the tectonic and rheological evolution in the regional geological context (e.g., Haertel et al., 2013; Kidder et al., 2018; Stipp et al., 2002).

Supervision: Michel Bestmann
Validation: Michel Bestmann, Giorgio Pennacchioni, Bernhard Grasemann
Visualization: Michel Bestmann
Writing – original draft: Michel Bestmann
Writing – review & editing: Michel Bestmann, Giorgio Pennacchioni, Bernhard Grasemann, Benjamin Huet, Michael W. M. Jones, Cameron M. Kewish

Ti-in-qtz thermometry (TitaniQ) is potentially a powerful method to estimate the ambient conditions of quartz formation (Huang & Audétat, 2012; Thomas et al., 2010; Wark & Watson, 2006). Under static conditions, Ti incorporation into the quartz lattice during crystal growth is a function of temperature, pressure and Ti activity. TitaniQ is well suited to quartz growth in magmatic and high-grade metamorphic rocks, and when quartz directly precipitated from a fluid.

The concentration of Ti, [Ti], in quartz can be modified during crystal-plastic deformation. This gives TitaniQ the potential of estimating the ambient conditions of deformation. Since the original proposal by Kohn and Northrup (2009), numerous studies have applied the TitaniQ to natural quartz-rich mylonites (Behr & Platt, 2011; Bestmann & Pennacchioni, 2015; Grujic et al., 2011; Haertel et al., 2013; Kidder et al., 2013, 2018; Korchinski et al., 2012; Nachlas et al., 2014; Pennacchioni et al., 2010). In addition, deformation experiments (Nachlas et al., 2018; Nachlas & Hirth, 2015; Negrini et al., 2014) have been conducted to understand the behavior of Ti in quartz in a dynamic context. These studies have shown that the [Ti] is influenced by several parameters: the recrystallization processes (Haertel et al., 2013), the amount of finite strain (Bestmann & Pennacchioni, 2015), strain/stress partitioning, fluid percolation and redistribution (Bestmann & Pennacchioni, 2015; Nachlas et al., 2014), and the metamorphic path (e.g., prograde vs. retrograde: Negrini et al., 2014).

Several studies have highlighted the difficulty of using TitaniQ as a robust geothermometer. Studies of natural quartz mylonites have suggested that the recrystallization mechanism has a primary effect on Ti re-equilibration in quartz during mylonitization. Grain boundary migration (GBM: Hirth & Tullis, 1992) recrystallization appears to be more efficient in Ti re-equilibration than subgrain rotation (SGR) recrystallization, especially at relatively lower temperatures (e.g., Grujic et al., 2011; Haertel et al., 2013; Nachlas et al., 2014). In particular, constraining the efficiency of [Ti] re-equilibration, during dislocation creep and SGR recrystallization, is challenging (Grujic et al., 2011; Haertel et al., 2013). Quartz deforms over a wide range of temperatures and strain rates in nature (e.g., Hirth & Tullis, 1992; White, 1976; Yund & Tullis, 1991). Considering the sluggish, intra-crystalline Ti diffusion in quartz over the temperature range where dislocation creep is predominant (Cherniak et al., 2007), strain-induced resetting of [Ti] is clearly enhanced by the grain size decrease (increase of reactive grain boundary area per unit volume) during SGR recrystallization. In fact, this process results in reduction of diffusion lengths for re-equilibration and provides pathways for fluids to access the grain interior (Ashley et al., 2014). However, commonly during dislocation creep, [Ti] is not completely reset (re-equilibrated) with respect to ambient conditions, resulting in highly heterogeneous [Ti] distribution across the strain gradients of quartz mylonites (Bestmann & Pennacchioni, 2015). Heterogeneities in [Ti] re-equilibration occur between microstructural domains of apparently similar finite strain and [Ti] also remains heterogeneous in pervasively deformed and recrystallized quartz mylonites. This reflects the complexity of the microstructural evolution of coarse-grained quartz aggregates with diverse crystallographic orientations in different crustal rocks, for example, in granitoids or pure quartz veins (Ceccato et al., 2017).

The use of TitaniQ, in quartz mylonites that underwent heterogeneous deformation in the dislocation creep regime requires identification of the sites of most complete syn-kinematic [Ti] re-equilibration. These sites do not necessarily correspond to the most strongly deformed domains. Due to the fact that [Ti] directly correlates with the cathodoluminescence (CL) intensity in quartz (e.g., Spear & Wark, 2009; Wark & Spear, 2005), large-area CL mosaic-imaging is the base to identify re-equilibration microstructures in combination with a rigorous protocol of integrated, high-resolution analysis by optical microscopy, electron backscatter diffraction (EBSD) and direct measurement of [Ti] using secondary ion mass spectrometry (SIMS). SIMS measurements are necessary for quartz deformed under middle to upper crustal conditions since the equilibrated [Ti] is commonly below the ~7 ppm detection limit of electron probe microanalysis (Nachlas et al., 2018).

Integration of the information from the different techniques is not only functional to TitaniQ thermobarometry, but also provides a robust tool for interpreting the interplay between grain-scale deformation, fluid-rock interaction, geochemical exchange and the evolution of the crystallographic preferred orientation (CPO) during increasing strain in a quartz mylonite. We present specific microstructures of deformed quartz veins from the Prijakt Nappe (Austroalpine Unit of Eastern Alps, Austria) as a key-study to unravel characteristic deformation processes responsible for partial to complete resetting of the Ti-in-quartz system toward lower concentrations under retrograde deformation condition in the SGR regime.

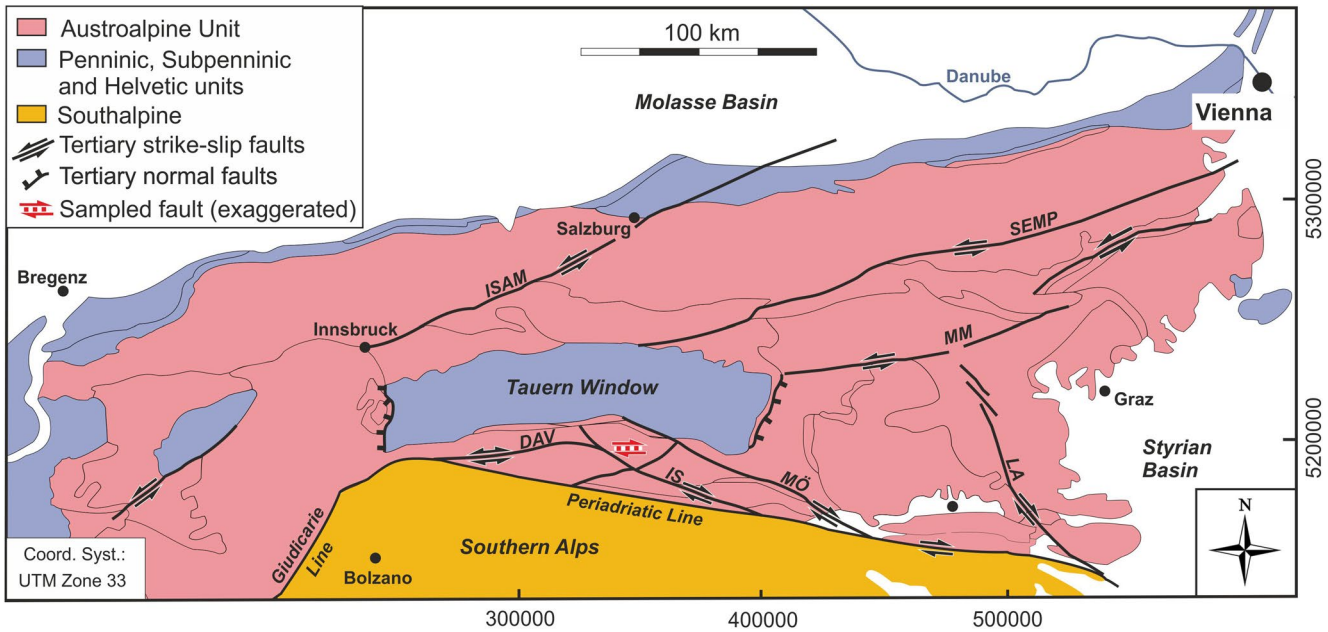

Figure 1. Simplified geological map of part of the Eastern Alps (modified after Schuster et al., 2014). Important Tertiary fault systems are given. Note sampled fault (red stippled line) is a continuation in strike of the Defereggental-Anterselva-Valles fault (DAV). Innsbruck-Salzburg-Amstetten fault (ISAM); Salzach-Ennstal-Mariazell-Puchberger fault (SEMP); Mur-Mürztal fault (MM); Lavanttal fault (LA); Mölltal fault (MÖ); Iseltal fault (IS).

2. Geological Settings

The samples analyzed in this study are deformed quartz veins (2–10 cm thick) that were collected within pre-Alpine paragneisses of the Austroalpine Prijakt Nappe of the Eastern Alps, Austria (Figure 1) (Krenn et al., 2012; Schulz, 1993). This nappe underwent Cretaceous subduction to eclogite-facies conditions at 650°C and 1.9 GPa (Hauke et al., 2019). The quartz veins crosscut eclogitic foliation and are deformed under amphibolite-facies conditions, locally forming flanking structures. Conditions of $T = 510–590°C$ and $P = 0.5–0.6$ GPa were constrained by multiequilibrium thermobarometry for the amphibolite-facies assemblage garnet-plagioclase-biotite-muscovite in paragneiss and orthogneiss (Linner, 1999).

In Oligocene-Miocene time, the tectonics of the Eastern Alps was dominated by the indentation of the Southern Alps, delimited by the Giudicarie and the Periadriatic fault systems (Figure 1), into the Eastern Alps. Indentation was accommodated within the Alpine stack by lateral escape, associated with the activity of a network of regional to smaller scale strike-slip faults (Mancktelow et al., 2001) and exhumation of the Tauern Window (Ratschbacher et al., 1989; Rosenberg et al., 2007). Prior to intrusion of the main Periadriatic plutons at ~30 Ma the shear sense on W-E-striking faults was sinistral. The transition from sinistral to dextral kinematics is related to the displacement along the Periadriatic fault, which continued at least until 13 Ma (Mancktelow et al., 2001).

The studied mylonitic quartz veins are associated with a W-E-striking steeply dipping strike-slip fault with a strike-length of ca. 500 m (UTM33 326383E/ 5199000 and 326674E/5199000N). For most of its length, the fault consists of an up-to-2 m wide zone of cataclasites, ultracataclasites and pseudotachylytes. The cataclastic rocks locally display an SCC' fabric consistent with dextral strike-slip (Figures 2c and 2d). The fault crosscuts the host rock eclogitic metamorphic foliation and folds. Toward the eastern extension of the fault zone (where the studied samples come from), the cataclasites and pseudotachylytes disappear and the dm-thick foliation-parallel quartz veins acted as tabular weak heterogeneity (Pennacchioni & Mancktelow, 2018) to localize dextral ductile shear (Figure 2a). Mylonitization of the quartz veins only occurs within a narrow zone of approximately 4–5 m along the fault trace. Quartz veins outside this zone are not deformed.

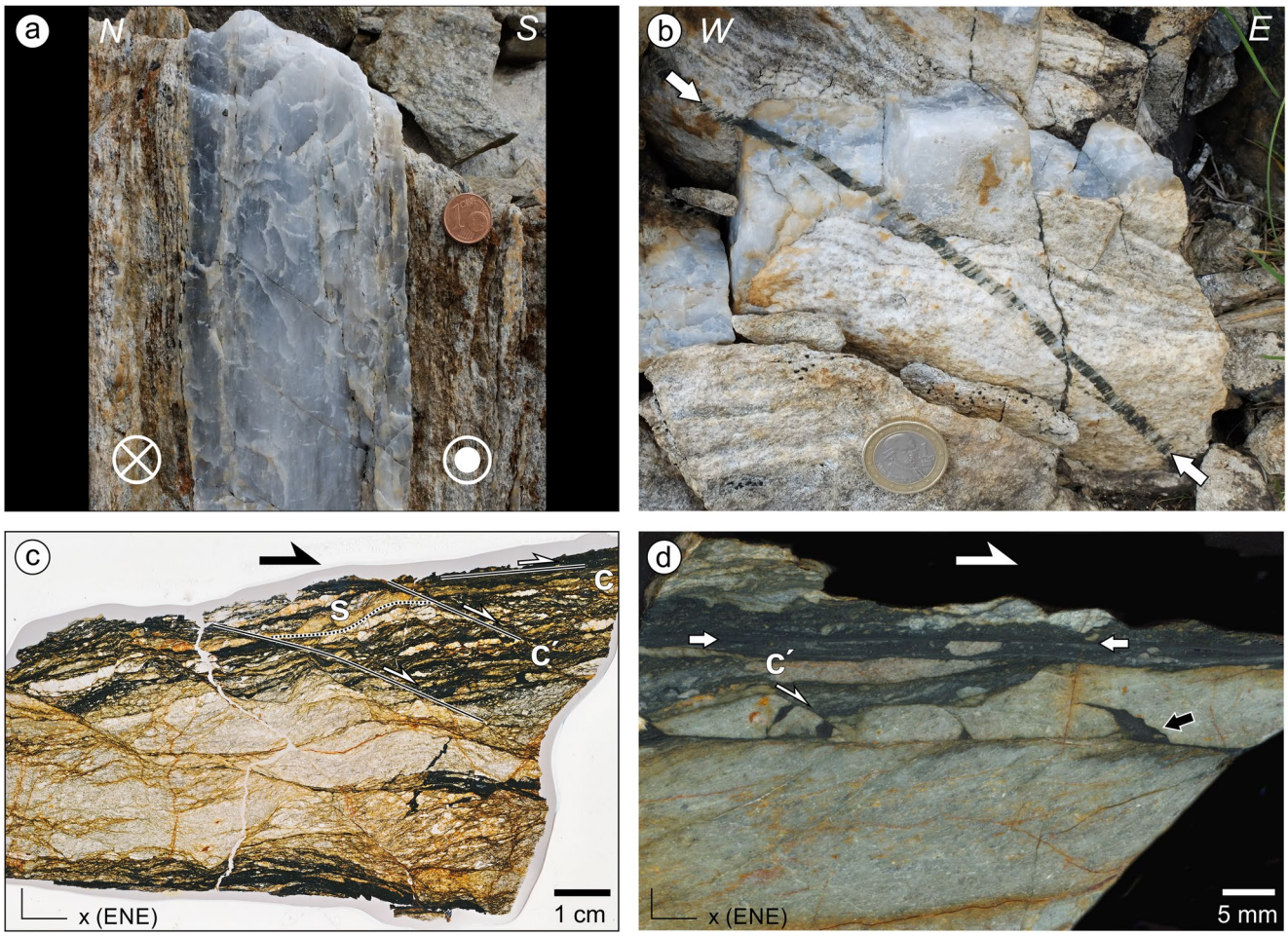

Figure 2. Field and sample pictures of the quartz mylonites and the brittle/ductile fault rocks. (a) Vertical, 7.5 cm-thick, mylonitic quartz vein within the foliated paragneisses (looking in the stretching lineation direction). Note the absence of cataclastic deformation. The white circle with the dot and with the cross indicates movement toward and from the observer respectively, accommodated by the quartz mylonite (UTM33 326551 E/ 5198986 N). (b) Fibrous quartz/chlorite vein (white arrows) cross-cutting the paragneiss and a mylonitized quartz vein oblique to the host rock foliation (UTM33 3265401 E/5198974 N) (see also Figure S6c in Supporting Information S1). (c) Scan of a large thin section of foliated cataclasites and pseudotachylytes, overprinted by dextral SCC' fabric (UTM33 326551 E/ 5198986 N). (d) Polyphase ultracataclasites/pseudotachylytes. Black arrow shows pseudotachylyte injection vein. Two small white arrows highlight a principal slip surface with a truncated grain, separating different generations of ultracataclasites/pseudotachylytes (UTM33 326542 E/ 5198982N). White half arrow marks C' plane.

3. Materials and Methods

The quartz vein analysis was conducted on thin sections (X-Z sections) oriented orthogonal to the vein boundary (X-Y plane in the kinematic reference frame) and parallel to the stretching lineation (*X*-axis). The center of the pole figures representing the CPO corresponds to the shear zone kinematic vorticity axis (*Y*-axis).

The veins were analysed by optical microscopy, SEM-CL and EBSD to characterize the quartz microstructures and CPO across the weakly to strongly deformed domains extending parallel to the vein boundary. Based on CL images, used as a proxy of the [Ti] in quartz (e.g., Bestmann & Pennacchioni, 2015; Wark & Spear, 2005), microstructurally controlled measurements of [Ti] were carried out by SIMS. The correlation between [Ti] and intensity of the CL signal is corroborated by SIMS measurements. Wavelength spectral analysis demonstrate that the CL signal depends only on the single emission peak at 400–420 nm (Figure S1 in Supporting Information S1). Despite the very low [Ti] (0.1–4.7 ppm), CL was capable of imaging sub-ppm [Ti] variations. Because the highest CL intensities of weakly deformed quartz veins is preserved in stretched vein crystals within protomylonites and within porphyroclasts in mylonites, SIMS measurements were focused on these domains where the whole

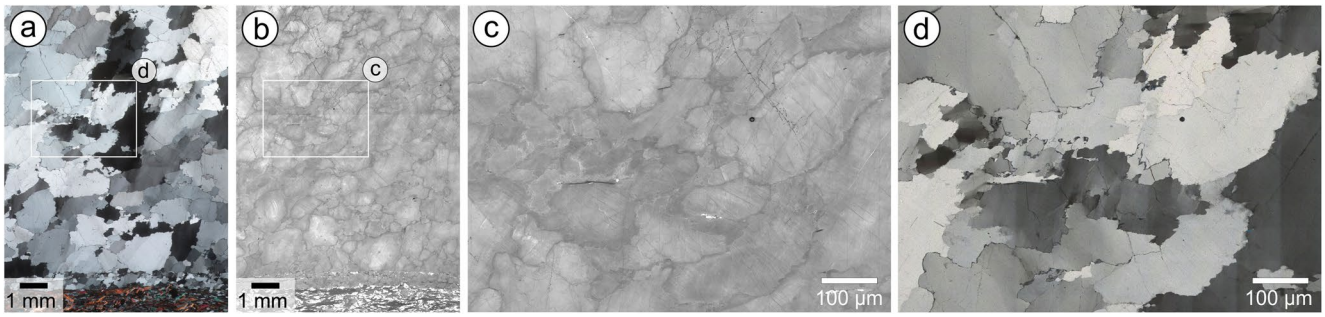

Figure 3. Weakly deformed quartz vein (sample HS-1B-2; UTM33 326621 E/ 5199004 N) showing coarse grains with lobate GB typical of grain boundary migration recrystallization related to the amphibolite facies deformation conditions after crystallization of the quartz veins. (a and d) Optical microphotographs under crossed-polarized light (XPL). (b and c) SEM-CL images of same area as (a) and (d).

range of CL/[Ti] variations are present across the diverse microstructures. Synchrotron-based X-ray fluorescence microscopy (XFM) was undertaken on the XFM beamline at the Australian Synchrotron (Howard et al., 2020) to identify a µm-sized Ti-bearing phase (rutile) within the vein that buffered the Ti activity.

High-resolution SEM channeling contrast (orientation contrast - OC) images, in combination with backscatter orientation contrast (BSE-OC) images and optical images in transmitted plane-polarized light, were used to record the variation of spatial density of small-scale (mostly <1 µm in diameter) pores mostly along (sub)grain boundaries. BSE images, energy-dispersive X-ray spectra and Raman spectra do not show any secondary mineral associated with the grain-boundary "specks" and supports that these specks are effectively pores. In the protolithic quartz grains, fluid inclusions with a vapor bubble are locally observed. In the deformed parts of the mylonitic quartz veins, the largest grain boundary pores (a few micrometers in diameter) also include submicron-sized bubbles indicative that these pores are effectively filled with fluid. The local, regular geometric arrangement of these grain boundary pores is typical of fluid-related etch pit porosity (Mancktelow & Pennacchioni, 2004). In the following we use the term grain boundary (GB) pores for these fluid-related microstructures. We used the relative variation of the spatial density of GB pores, in combination with the resetting of the CL intensity and decreasing [Ti], as a proxy of the fluid distribution across the microstructure. The composition of syn- and late-mylonitic chlorite was determined by microprobe analysis in order to apply chlorite thermometry (Vidal et al., 2005, 2006) as an independent, complementary estimate of temperature to TitaniQ. A description of the analytical apparatus and procedures used in the study is reported in the Supporting Information S1.

4. Results

Weakly deformed domains consist of mm-sized vein crystals (qtz_1; Figure 3). Most veins show a strain increase toward the vein core or from one vein margin (protomylonite) to the other (ultramylonite; Figures 4a and 4b). With increasing strain, qtz_1 grains were progressively stretched, with their long axis rotated toward the shear plane (vein boundary) and dynamically recrystallized to different degrees depending on their crystallographic orientation. Some qtz_1 grains persist as porphyroclasts in the extensively recrystallized qtz_2 ultramylonite (Figures 5–8). Elongated qtz_1 grains, with internally highly elongated subgrain domains, recrystallized into elongated (up to 10:1 aspect ratio; over one hundred microns long) new grains (qtz_{2A}) (Figure 9). During ongoing deformation the highly sub-structured qtz_{2A} grains develop new smaller grains (qtz_{2B}) at their margin by subgrain rotation recrystallization. These new mantle grains are only slightly elongated (maximal aspect ratio of 2:1) and the grains size (1–10 µm) is in the same range as the marginal subgrains of the elongated qtz_{2A} grains (Figures 9f and 9g). At high strain, the microstructure is still heterogeneous: the main foliation, parallel to the vein boundary, is defined by the alternation of dominant, recrystallized layers showing a distinct internal extinction banding (100–500 µm in thickness) and monocrystalline (commonly highly sub-structured) ribbon grains (Figure 10). The recrystallized layers show a CPO with a single *c*-axis girdle and variable sub-maxima resulting in the optical extinction banding

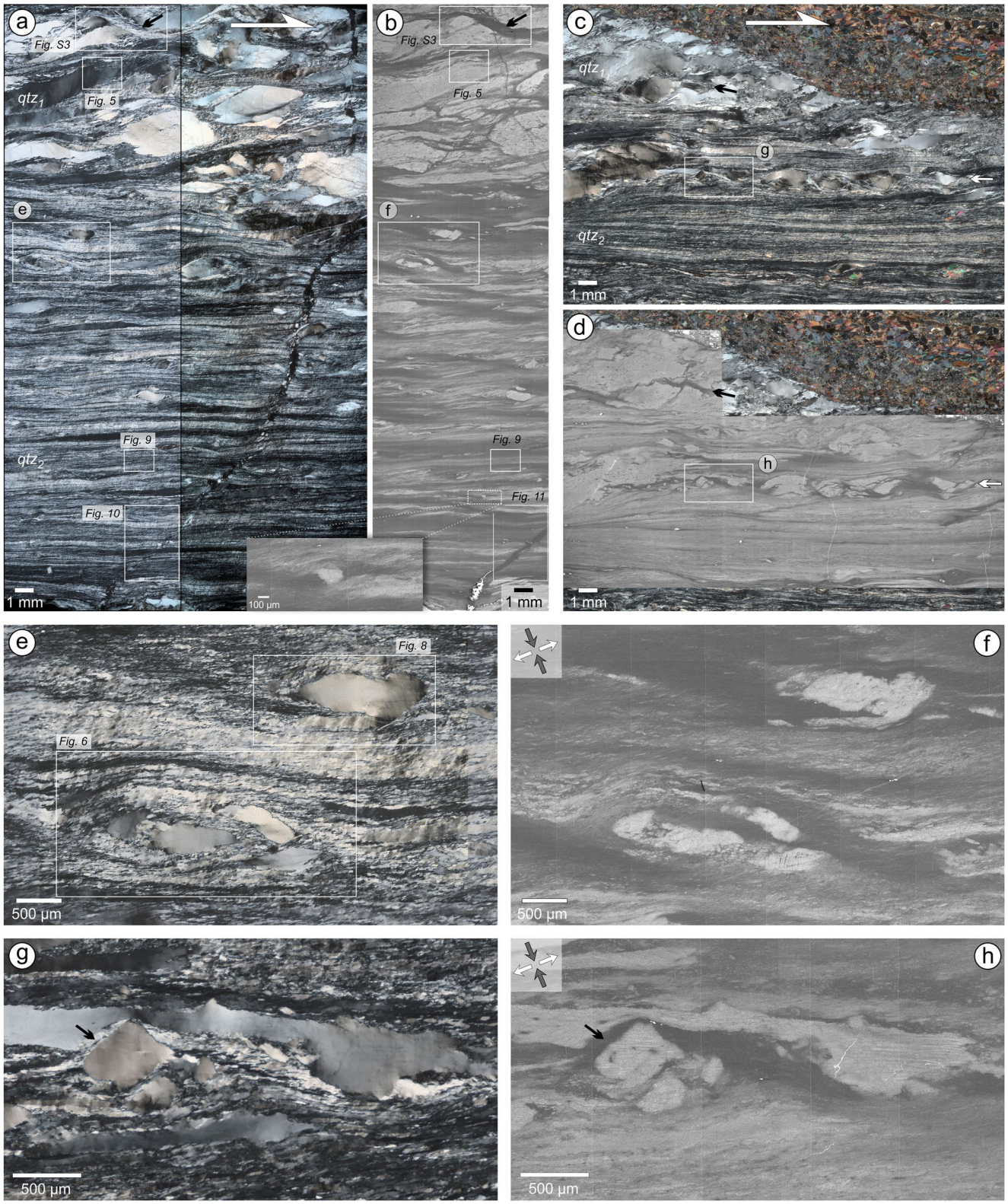
a
Fig. S3
qtz1
Fig. 5
e
Fig. 9
qtz2
Fig. 10
1 mm
100 µm
b
Fig. S3
Fig. 5
f
Fig. 9
Fig. 11
1 mm
c
qtz1
g
qtz2
1 mm
d
h
1 mm
e
Fig. 8
Fig. 6
500 µm
f
500 µm
g
500 µm
h
500 µm

Figure 4.

(Figure 9d and 10c-II). Quartz (qtz_3 ±chlorite) veins, only slightly involved in ductile deformation, crosscut the foliation of deformed quartz veins at a high angle (Figures 2b, 11 and 12). The microstructural and CPO evolution, and the variations in [Ti] across the differently strained domains (imaged by CL and measured by SIMS) are described in detail below.

4.1. Weakly to Moderately Deformed Quartz Vein Domains

The least deformed quartz veins contain mm-sized crystals (qtz_1) (Figure 3). These crystals contain deformation bands, elongated subgrains and deformation lamellae, and show serrate grain boundaries (GB). The CL shade of qtz_1 varies from medium to light gray with darker tones at GB, likely indicative of growth zonation (over a thickness of 20–40 µm; Figures 3b and 3c). XFM element maps reveal dispersed inclusions of rutile grains (3–7 µm grain size) in qtz_1 and along pristine microshear zones (Figure S2 in Supporting Information S1).

With increasing bulk strain qtz_1 grains become (i) stretched to different degrees, depending on their crystallographic orientation relative to the kinematic reference frame, and (ii) separated by microshear zones of recrystallized grains (qtz_2; Figure 5a, Figure S3 in Supporting Information S1). Qtz_1 grains show a high spatial density of low angle boundaries (LAB: misorientations <10–15°; Figure 5f). In qtz_1 grains with *c*-axis oriented between the *Y* and *Z*-axis, the LAB misorientation axis plot shows clustering around <*c*> with a spread to the rhomb planes and to the {10–12} direction (Figure 5g). Qtz_1 grains with a peripheral *c*-axis orientation in the pole figure have more random LAB misorientation axes and higher degree of recrystallization (e.g., Figure 8e). As a characteristic example of elongated qtz_1 domains, the selected grain (aspect ratio of 10:1) of Figure 5, with *c*-axis inclined 37° to the *Y*-axis in the Y-Z plane, is highly substructured. The LAB misorientation axes cluster around <*c*> (Figure 5g) and the pole figure shows a continuous dispersion path around the {10–12} pole close to the *Y*-axis (Figure 5g). This qtz_1 grain has a similar CL shade as the incipiently deformed quartz vein crystals (Figures 5b and 5e). In contrast, the recrystallized portions are darker in CL shade (Figure 5e), and are associated with high angle boundaries (HAB: misorientation >10–15°; Figures 5f and 5j) and grain boundary pores (Figures 5i and 5j). The interior of qtz_1 grain shows a network of thin dark gray lines in CL (Figure 5e) that matches the LAB network (misorientation 0.5°–15°) of EBSD maps (Figure 5f) and the OC image (Figure 5h). There are nearly no pores associated with LAB in either the optical (Figure 5i) or the BSE-OC images (Figure 5k).

4.2. Strongly Deformed Domains

Strongly deformed vein portions show a mylonitic foliation subparallel to the vein boundary defined by the alternation of layers of (a) dominant, recrystallized aggregates of $qtz_{2A,B}$ with slightly different CPO reflected in the extinction banding, and (b) monocrystalline, ribbon grains (Figure 10). This layering is partially reflected in a CL shade layering (Figure 11a). The foliation wraps around local, mm-sized qtz_1 porphyroclasts (Figure 4). In the following we highlight the correlations between the CL patterns and [Ti], and the CPO, (sub)grain size and porosity distribution.

4.2.1. Qtz_1 Porphyroclasts

Most qtz_1 porphyroclasts within the (ultra)mylonite have a nearly peripheral *c*-axis orientation in the pole figure, slightly rotated to the *Z*-axis (e.g., Figure 8e, Figure S4h in Supporting Information S1). Two microstructural sites (*Site 1*, *2*) of sample MS-H2-2 (Figure 4e) were selected for detailed study.

Figure 4. Microstructures (optical microphotograph, XPL, and corresponding CL images) of two deformed quartz vein samples (a, b, e, f: sample MS-H2-2; c, d, g, h: sample MS-09a - UTM 33 326551 E/5198986). Both samples show a strain gradient from a protomylonitic fabric (upper part) to mylonitic/ultramylonitic fabric (lower part). The latter reveals a characteristic extinction banding in the optical images (a and c). MS-H2-2 shows a corresponding banding in the CL image (b). The (ultra) mylonitic part of MS-09a reveals similar CL intensity as the coarse qtz_1 clasts with only subtle variations (d). (e–h) Microstructures of quartz clasts in (ultra)mylonitic qtz_2 matrix. Note in (f), the CL intensity variation around the lower left clast-aggregate corresponding to stress-field–four-quarter pattern. Similar 4-quadrand CL feature is highlighted in (b) – see inset. For both samples the schematic (not quantified) orientation of the instantaneous stretching axis is given in (f and h) – see inset. In (a and b), (c and d) and (f and h) examples of microshear zones are marked by black arrows which show evidence of channelization of fluid indicated by dark CL signal (see text and Figure S3 in Supporting Information S1). In (c and d) white arrows mark clasts aligned in the mylonitic matrix as an example for [Ti]/CL resetting related to the combination of fluids trapped in dilatation sites and/or strain shadows and channeled in microshear zones (see text in Section 5.2.1.2). The sense of shear is dextral in all the figures.

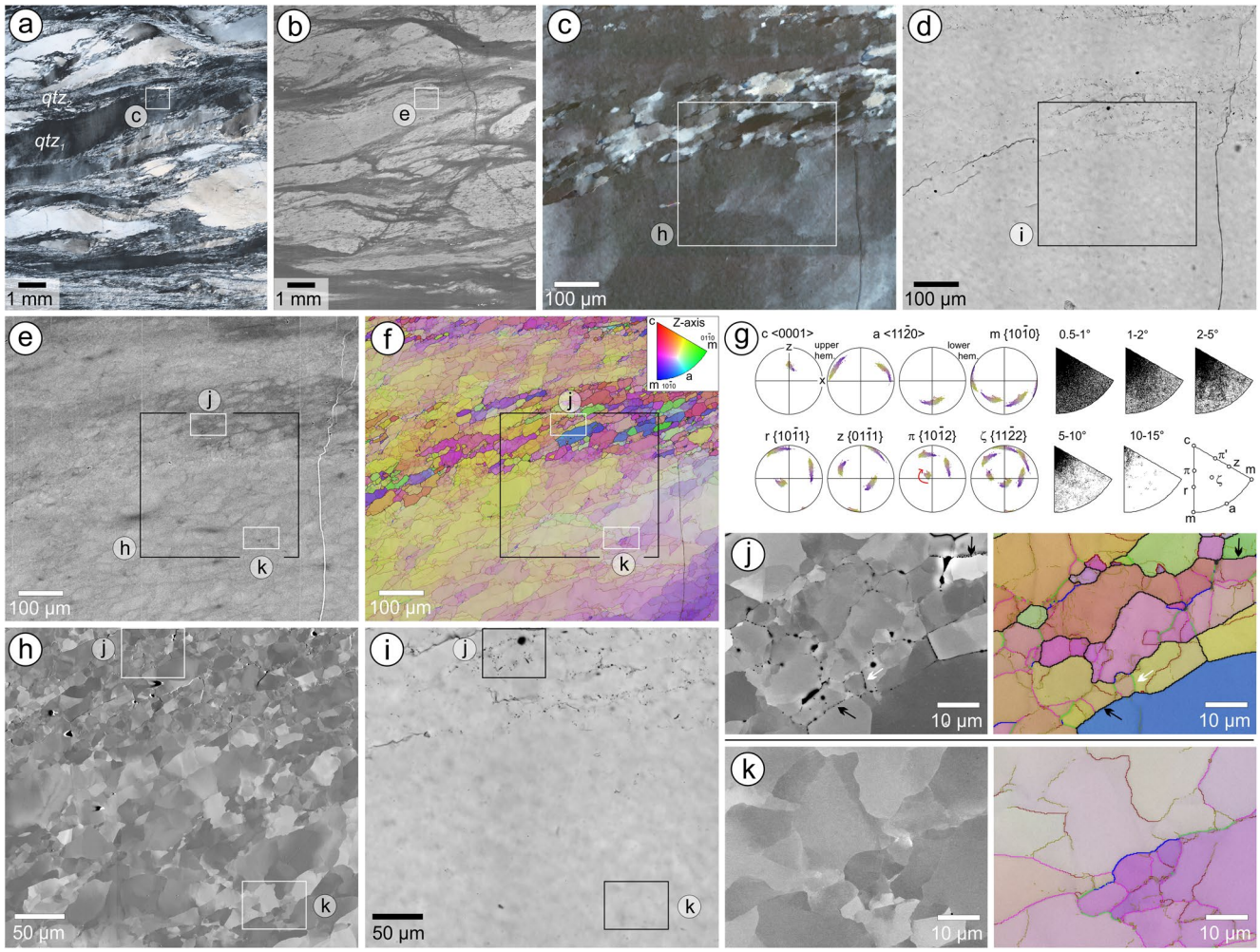

Figure 5. Internal deformation microstructure of elongated quartz grain (qtz_1). (a and b) Protomylonitic part of sample MS-H2-2 (XPL, SEM-CL). Note, network of microshear zones and accompanied darker CL shades in (b). (c–f) Enlarged microstructure as marked in (a and b) – same location site (c: optical microphotograph, XPL; d: optical microphotograph under plane-polarized light, PPL; e: SEM-CL; f: EBSD orientation map (step size: 200 nm) color coded with respect to Z-axis of the pole figure – see inset). For boundaries levels see key below. Note that high spatial density of fluid-related pores in (d) matches with dark CL patterns in (e). In (e) fine dark-gray CL lines correspond to low angle boundaries (LAB) in (f). (g) Pole figures (PF, equal area, lower hemisphere projection) and inverse pole figures (IPF) with respect to crystal references system (equal area, upper hemisphere projection) of substructured host crystal (lower half of EBSD map) without new grains. (h) Orientation (channeling) contrast (OC) image of area as marked in c, e, f. (i) Optical microphotograph (PPL) of same area as in (h). (j and k) Detailed backscatter orientation contrast (BSE-OC) images and EBSD maps of areas as marked in e, f, h, i. Note, in (j) the porosity (dark spots in the BSE-OC images) corresponds to the fluid-related pores in (i) and mainly follows high angle boundaries (HAB, black arrows) of smaller new grains, and less frequently along low angle boundaries (LAB, white arrows) - see EBSD maps. In contrast, the subgrain microstructures within the elongated quartz grain (k) does not contain significant porosity. EBSD boundary levels (misorientation angle interval): low angle boundaries: olive green 0.5–1°, maroon 1–2°, fuchsia 2–5°, green 5–10°; high angle boundaries: blues 10–15°, black >15°; Dauphine twin: red 60° ± 5° around <*c*> axis.

Site 1 (Figure 6) shows a cluster of qtz_1 porphyroclasts (I-IV) mostly retaining the CL shade of qtz_1 characteristic of the weakly deformed vein portions (see also Figure 4a, 4b, 4e and 4f). The presented [Ti] of 3.6–4.1 ppm (*SIMS-profiles 8–11*, *13*, *14*) correlates with the CL variation. Fluid inclusions are rare or absent within clasts (Figures 6d and 6g and 7). As a whole the cluster defines a composite low-strain domain with the wrapping recrystallized qtz_2 matrix showing variation of CL shade between the contractional and extensional domains, induced by distortion in the non-coaxial (dextral) flow, at opposite quarters of the porphyroclast cluster (Figure 6a) (Hanmer & Passchier, 1991). The contractional domains show medium-dark CL shade and 1.3–2.7 ppm [Ti] (*SIMS-profiles 10*, *15*). The extensional quarters, including the recrystallized domain between I and III, show darker CL shade and 0.4–0.5 ppm [Ti] (*SIMS-profiles 7*, *12*). These CL/[Ti] patterns well correlate with the density of HAB grain boundary pores; higher in the Ti-poorer extensional domains (Figures 6a and 6d) and lower in the Ti-richer clasts (Figure 7). The separation zone between porphyroclasts I and II shows heterogeneous CL

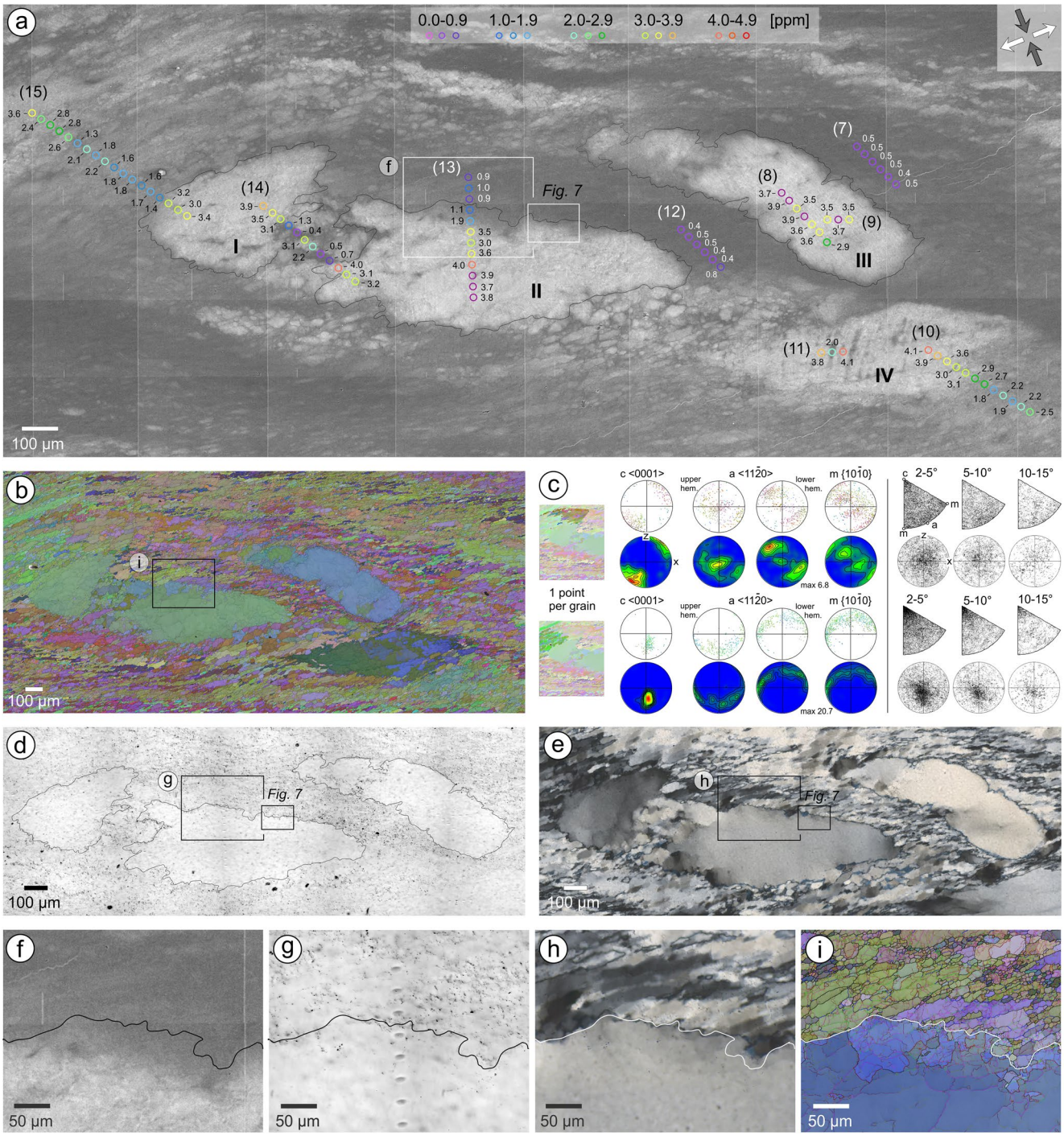

Figure 6. *Site 1*, cluster of qtz_1 porphyroclasts (I-IV) within (ultra)mylonitic matrix as marked in Figure 4e. (a) SEM-CL image with Ti-in-qtz data. SIMS analysis spots (c. 15 µm) are color-coded with respect to Ti concentration [Ti] – key is given. (b) EBSD map (step size: 500 nm) color coded with respect to Euler angles. Internal substructure is highlighted by superposition of transparent Euler map on the band contrast map. (c) Variation of the CPO of (ultra)mylonitic flow fabric around clast. Orientation data of two specific areas are plotted as pole figures (left column; density maxima are given as multiple of random distribution, *mrd*) and misorientation axis plots (right column) of LAB (inverse pole figure: crystallographic reference system; pole figures: sample reference system). (d, e) Optical microphotographs (PL, XPL). Note, the spatial density of fluid-related GB pores correlates with CL variation in (a). (f–i) Porphyroclast II: magnification of the porphyroclast margin outlined in a–e. Black lines indicate grain boundary (GB) of quartz clast. In (f) decreasing CL intensity in clast toward GB corresponds to higher subgrain boundary (SGB) density shown in (i), whereas the SGB density is relatively low (g). In (d) and (g), the line of spots corresponds to the SIMS analyses. (i) Clast in EBSD orientation map is color coded with respect of texture component in blue, surrounding recrystallization matrix to Euler angles. Boundary level coding follows Figure 5.

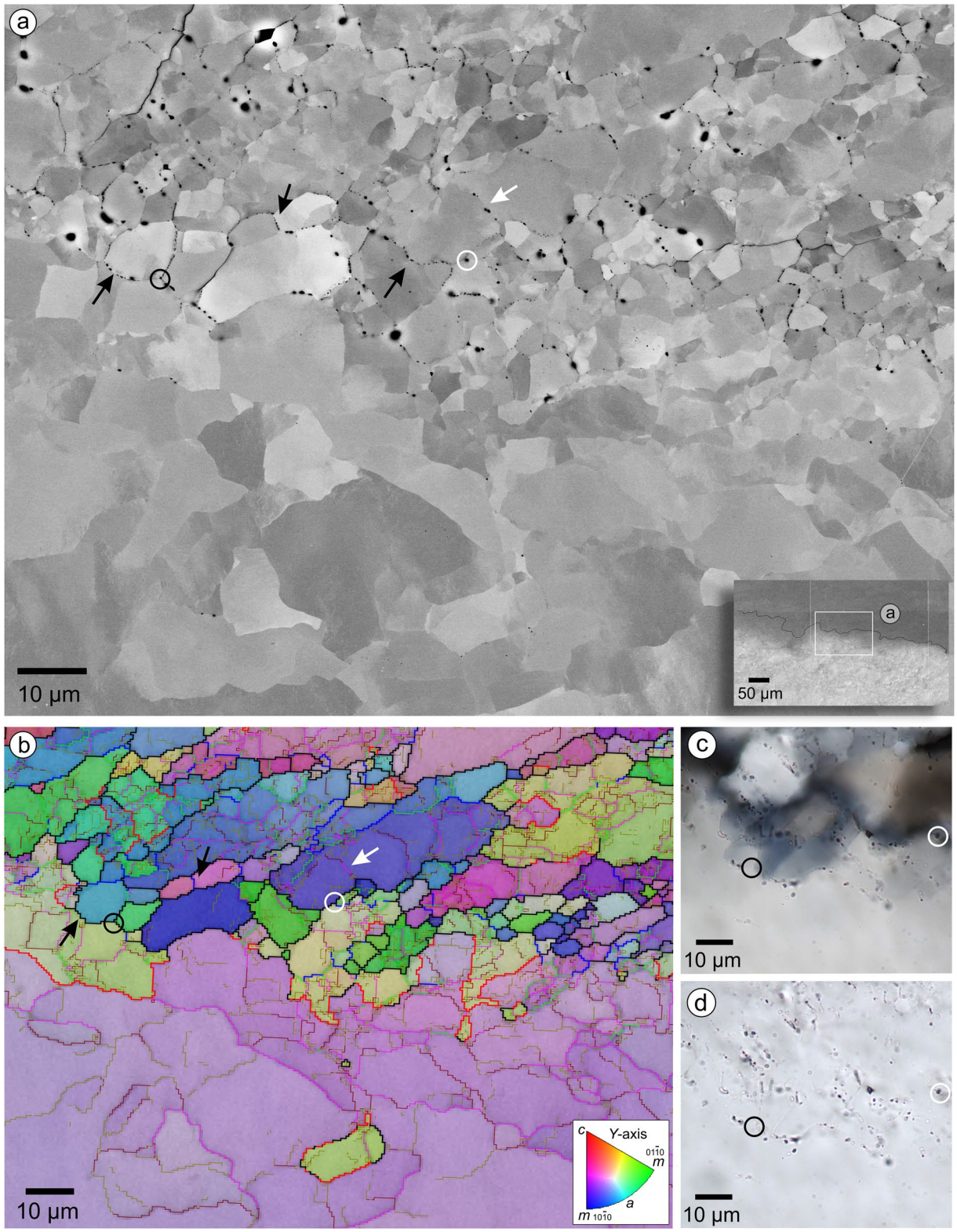

Figure 7. Density distribution of fluid-related GB pores between recrystallization matrix and porphyroclast II of *Site 1* as marked in Figure 6. (a) Backscatter orientation contrast (BSE-OC) image of area marked in CL image - see inset. (b) EBSD map of same area as in (a) (step size 500 nm). Orientation data are color-coded with respect to the *Y*-axis of the pole-figure - see inset. Boundary level coding follows Figure 5. (c–d) Optical micrographs (PL, XPL). Open circles mark same positions in the images (a–d). Fluid-related pores mainly follows HAB (black arrows) and less frequently along LAB (white arrows) of smaller new grains (upper part of a and b). LAB in the porphyroclast are nearly free of pores.

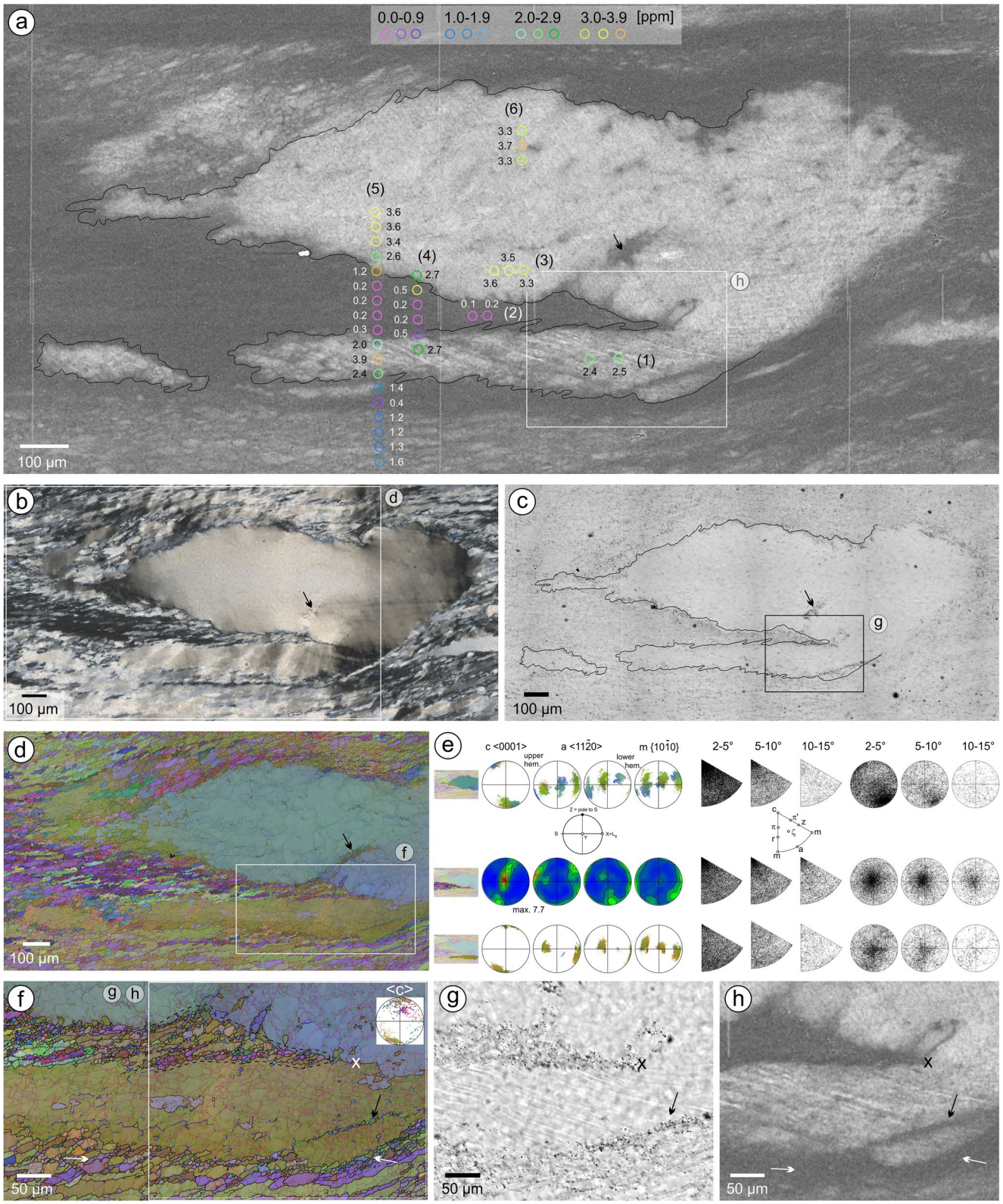
a
0.0-0.9 1.0-1.9 2.0-2.9 3.0-3.9 [ppm]
(6)
3.3
3.7
3.3
(5)
3.6
3.6
3.4
2.6
1.2
0.2
0.2
0.2
0.3
2.0
3.9
2.4
(4)
2.7
0.5
0.2
0.2
0.5
2.7
3.5
(3)
3.6
3.3
0.1
0.2
(2)
2.4
2.5
(1)
h
1.4
0.4
1.2
1.2
1.3
1.6
100 µm
b
d
100 µm
c
g
100 µm
d
f
100 µm
e
c <0001>
a <11$\bar{2}$0>
m {10$\bar{1}$0}
upper hem.
lower hem.
Z = pole to S
max. 7.7
2-5°
5-10°
10-15°
2-5°
5-10°
10-15°
f
g h
<c>
x
50 µm
g
x
50 µm
h
x
50 µm

Figure 8.

and [Ti] patterns (*SIMS-profile 14*) with (i) larger irregular portions, partially retaining the typical CL shade of qtz_1, and (ii) CL-darker domains (Figure 6a and in detail Figure S4 in Supporting Information S1). (a) The former are highly sub-structured, contain scarce GB pores and show a trend of decreasing [Ti] (1.3–2.2 ppm) from the values of the porphyroclast cores. (b) The CL-darker domains include new qtz_2 grains (with similar orientation as the qtz_1 porphyroclasts I & II, Figure S4h in Supporting Information S1), have higher spatial density of GB pores (Figure S4 in Supporting Information S1) and show lower [Ti] (0.4–0.7 ppm). Porphyroclast II locally shows a progressively darker CL shade toward the rim (up to 50 µm in width; Figure 6f in Supporting Information S1), in association with highly sub-structured domains (Figure 6i in Supporting Information S1) almost free of pores (Figure 6g in Supporting Information S1). This corresponds to a progressive decrease of [Ti] from 3.0-4.0 ppm (clast interior) to 1.1 ppm (clast margin) (Figure 6a in Supporting Information S1, *SIMS-profile 13*). [Ti] decreases to 0.9 ppm in the adjacent recrystallized qtz_2 aggregate rich in GB pores.

Site 2 (Figure 8) shows an isolated folded qtz_1 porphyroclast enclosing a wedge-shaped zone of recrystallized qtz_2 grains. The postulated fold structure, with a fold axis parallel to the stretching lineation (Bell & Hammond, 1984), explains the mirror orientation of the CPO in the two limbs (Figure 8e) and synthetic shearing in the recrystallized part between the two limbs. The general dextral shear sense is indicated by the oblique shape preferred orientation of qtz_2 grains (Figures 8b and 8d). The upper limb has moderate-light CL shade and 3.3–3.7 ppm [Ti] (*SIMS-profiles 3*, *5*, *6*). The presence of localized clusters of GB pores within the porphyroclast associated with darker CL shades is related to an intracrystalline zone of recrystallized grains (black arrows in Figures 8a–8d). The lower limb shows a more heterogeneous CL pattern corresponding to a larger variation in [Ti] (2.0–3.9 ppm; *SIMS-profiles 1*, *4*, *5*). The set of thin CL-brighter lines corresponds to deformation lamellae (Figures 8g and 8h). The wedge-shaped recrystallization qtz_2 zone shows homogenous dark CL shade, 0.2–0.5 ppm [Ti] (*SIMS-profiles 2*, *4*, *5*) and abundant GB pores (Figures 8c, 8g and 8h). Note, at the tip of the recrystallized zone, the dark CL pattern continuous several tens of micron along the HAB (between the two limbs) with no evidence of new recrystallized grains but with a high density of GB pores ("x" in Figures 8f–8h). The CPO of the recrystallized zone consists of an oblique, single girdle with *c*-axis *Y*-maximum and peripheral sub-maxima (nearly overlapping with the host grain CPO) linked to low-strain tip of the recrystallized zone with a host-controlled CPO related to the lower limb (Figure 8f). There is no noticeable change in CL shade within the porphyroclast associated with the strain gradient toward the tip of the recrystallized zone (Figures 8f–8h). A dark CL shade is also observed for very thin (single-grain-thick) microshear zones of recrystallized qtz_{2B} showing HAB porosity (Figures 8f–8h, black arrows). There is also no noticeable change in CL shade between recrystallized aggregates of qtz_{2A} and qtz_{2B} (Figures 8f and 8h).

4.2.2. Monocrystalline Lenticular Quartz

Qtz_1 grains are progressively stretched into lenticular, high aspect ratio, monocrystalline grains bending into the mylonitic foliation subparallel to the vein boundary (e.g., Figure 5a). Qtz_1 grains less favorably oriented for prism<*a*> slip (*c*-axis angle to *Y*: >54°) tend to recrystallize as soon as the clasts bend into the shear foliation (*ribbon-clast-1*, *2* in Figure 10a). This goes along with the overall change to darker CL shades associated with the appearance of a high spatial density of GB pores (Figure 11a). The recrystallized grains commonly contain CL-brighter remnant cores. Extensive recrystallization is especially observed for ribbon-clasts with *c*-axes at the pole figure periphery (*ribbon-clast-1*). Instead of a main clustering of LAB misorientation axis parallel to <*c*> a tendency around {*m*} is evident suggestive of basal<*a*> and/or ξ<*c*+*a*> slip (Neumann, 2000; Figure 10c-I). Deformation zones, showing different degree of recrystallization, are commonly localized between the rib-

Figure 8. *Site 2*, quartz clast within (ultra)mylonitic matrix as marked in Figure 4e. (a) SEM-CL image with Ti-in-qtz data. SIMS analysis spots (c. 15 µm) are color with respect to [Ti] – key is given. (b and c) Optical microphotographs (XPL, PL). Note, density of fluid-related GB pores in (c) corresponds with CL variation in (a). Black line in (a–c) indicates GB of quartz clast. (d) EBSD map (step size: 500 nm): transparent superposition of Euler and band contrast map. (a–d) Within the porphyroclast a localized cluster of fluid-related GB pores (b, c) associates with darker CL shades (a) and relates to an intracrystalline zone of recrystallized grains (d) (black arrows). (e) Orientation data of clast domains are presented as pole figures and misorientation axis plots of LAB (IPF and PF) – see Figure 6c. (f) Enlarged EBSD area as marked in (d). *C*-axis pole figure of recrystallized grains at the tip of the microshear zone is given – see inset. For Key of LAB and HAB see Figure 5. (g) Optical microphotograph (PPL) of area as marked in (f). (h) SEM-CL image of same area as presented in (g). CL variation corresponds to density of fluid-related GB pores shown in (g). In (f–h) black arrows mark intracrystalline deformation zone traced by HAB. White arrows mark recrystallization zone below the clast. "x" marks the position of the tip of the dark CL feature. Note, in the EBSD map (f) the location of "x" is several tenth of micron away from the recrystallized tip of the microshear zone and is located on the HAB between the upper and lower limb where no new recrystallized grains are developed. Oblique features in (g and h) are deformation lamellae.

bon-clasts. However, independently of the accommodated amount of strain, the localized zones reveal a resetting toward low CL intensities and low [Ti] (0.3–1.0/ 1.8 ppm; *SIMS-profile 13*, Figure 11a).

4.2.3. Quartz Ribbons

In general, quartz ribbons preserve a light CL shade similar to, or slightly darker than that of qtz_1 grains (Figure 11a). The corresponding [Ti] vary between 3.0 and 4.7 ppm (lighter ribbons: *ribbon-1*, *2*) and 1.6–3.2 ppm (darker ribbons: *ribbon-3*, *4*). All ribbons contain a high spatial density of LABs (Figures 11b-IV, Figure S5d in Supporting Information S1) with a main cluster of misorientation axes around <*c*> and additional sub-clusters toward {*r*}/{*z*} and {ξ}, even for misorientation angles >10–15° (Figure 10c-I *ribbon-4*). The internal HAB are mostly not interconnected. The cellular-structure with a brighter CL shade present within some ribbons (e.g., *ribbon-2*, Figure 11b) corresponds to LABs not associated with detectable [Ti] variations likely corresponding to intrinsic lattice defects of SGB (Hamers et al., 2017). Ribbons with the *c*-axis next to the *Y*-axis (*c*-axis angle to $Y \leq 25°$; *ribbon-2*) are the most elongated (up to 1 cm long and 250 µm thick; Figure 10a, c-I). The LAB misorientation axes are subparallel to <*c*> and correspond to prism<*a*> slip (Neumann, 2000). Ribbons with *c*-axis orientation between *Y* and *Z* (angle 40–44°) show a main clustering of LAB misorientation axes (sub)parallel to <*c*> but also toward {*r*} and {*z*}. This suggests the occurrence of both prism<*a*> and rhomb<*a*> slip (Neumann, 2000). These grains show a higher degree of recrystallization at their ends where the CL shade becomes darker. In general, ribbons are nearly free of porosity (Figures 10b-II, Figure S5c in Supporting Information S1), except for specific clusters and zones of incipient recrystallization.

4.2.4. Strongly Deformed, Pervasively Recrystallized Aggregates

Pervasively recrystallized aggregates are characterized by extinction banding and corresponding CL shade variations (layer thickness 100–500 µm; Figures 4a and 4b; 9a, b; 10a, 11a). The CPO of the different layers indicate a variation in the distribution of the *c*-axis sub-maxima within the *c*-axis girdle, mainly located between the *Y* and *Z* direction of the pole figures (Figure 9d and 10c-II). The distribution of LAB misorientation axes mainly clusters around <*c*> in the inverse pole figures (IPF; Figure 9d and 10c-II). We used the density distribution in the IPF (multiple of random distribution, *mrd*, for misorientation angle interval 2–10°) to quantify the activity of slip system, especially prism<*a*> when the highest cluster density is around <*c*> (Neumann, 2000). The *mrd* values of IPF varies for different CPOs (position of the *c*-axis sub-maxima). In general, the closer the *c*-axis sub-maxima to the *Y*-axis the higher the *mrd* of LAB misorientation axes in the IPF with a main clustering around <*c*> (Figures 10c-II). For some (ultra)mylonitic areas there is a tendency that layers with dark CL shade show higher *mrd* values, corresponding to *c*-axis clustering toward *Y*-axis (e.g., *mylonite-5* - dark CL, *mrd* 4.2; Figure 10c-II and 11a). Adjacent layers with a brighter CL signal are characterized by lower *mrd* values and more peripheral *c*-axis sub-maxima in the pole figures (*mylonite-3* and *6* – brighter CL, *mrd* 2.9 and 2.8; Figure 10c-II and 11a). The layers with darker CL shade commonly display a higher degree of smaller (sub)grain size and accompanied higher spatial density of GB pores than CL-brighter layers. However, this is not always true and no strict correlation between CL shade, CPO, misorientation axis distribution, (sub)grain size and density of GB pores can be demonstrated. For example, the ultramylonitic area in Figure 9a is completely recrystallized ($qtz_{2A,B}$) and shows extinction banding. The recrystallized layer with brighter CL shade (thickness 300 µm) (*layer-II* in Figure 9b) is surrounded by either sides by recrystallized layers with darker CL shade (*layer-I & III* in Figure 9b). However, the brighter CL *layer-II* shows a cluster of *c*-axes in the center of the pole figures (*Y*-axis), whereas the *c*-axis sub-maxima of the adjacent *layers-I* and *III* (dark CL) tend to localize further away from *Y* and/or a located near the pole figure periphery (Figure 9d). This is also reflected by the *mrd* values of the LAB misorientation axes (clustering around <*c*> in the IPF) showing higher values for *layer-II* (*mrd* 7.45) compared to the adjacent layers, *layer-I* (*mrd* 4.58) and *layer-III* (*mrd* 5.29). Further, all three layers show the same (sub)grains size distribution and there is no obvious variation of the spatial density of GB pores. Pores occur mainly along HAB but are also present along LAB (Figures 9f and 9g).

In sample *MS-09a* the strongly deformed vein portions show a characteristic extinction banding but a relatively minor corresponding variation in CL shade (Figures 4c and 4d). With respect to the protomylonitic part of the sample, the (ultra)mylonitic aggregate (recrystallized qtz_2 grains) has a similar CL shade which is only slightly reduced (Figure 4d). A strong reduction in the CL shade is only observed in strain shadows and microshear zones between coarse quartz clasts (arrows in Figure 4c, 4d, 4g and 4h). It is important to note that only the microstructures with a dark CL shade contain a high spatial density of GB pores. In contrast, the (ultra)mylonitic matrix with its relatively homogeneous, moderate CL shade is characterized by a very low density of GB pores, except very locally along HAB.

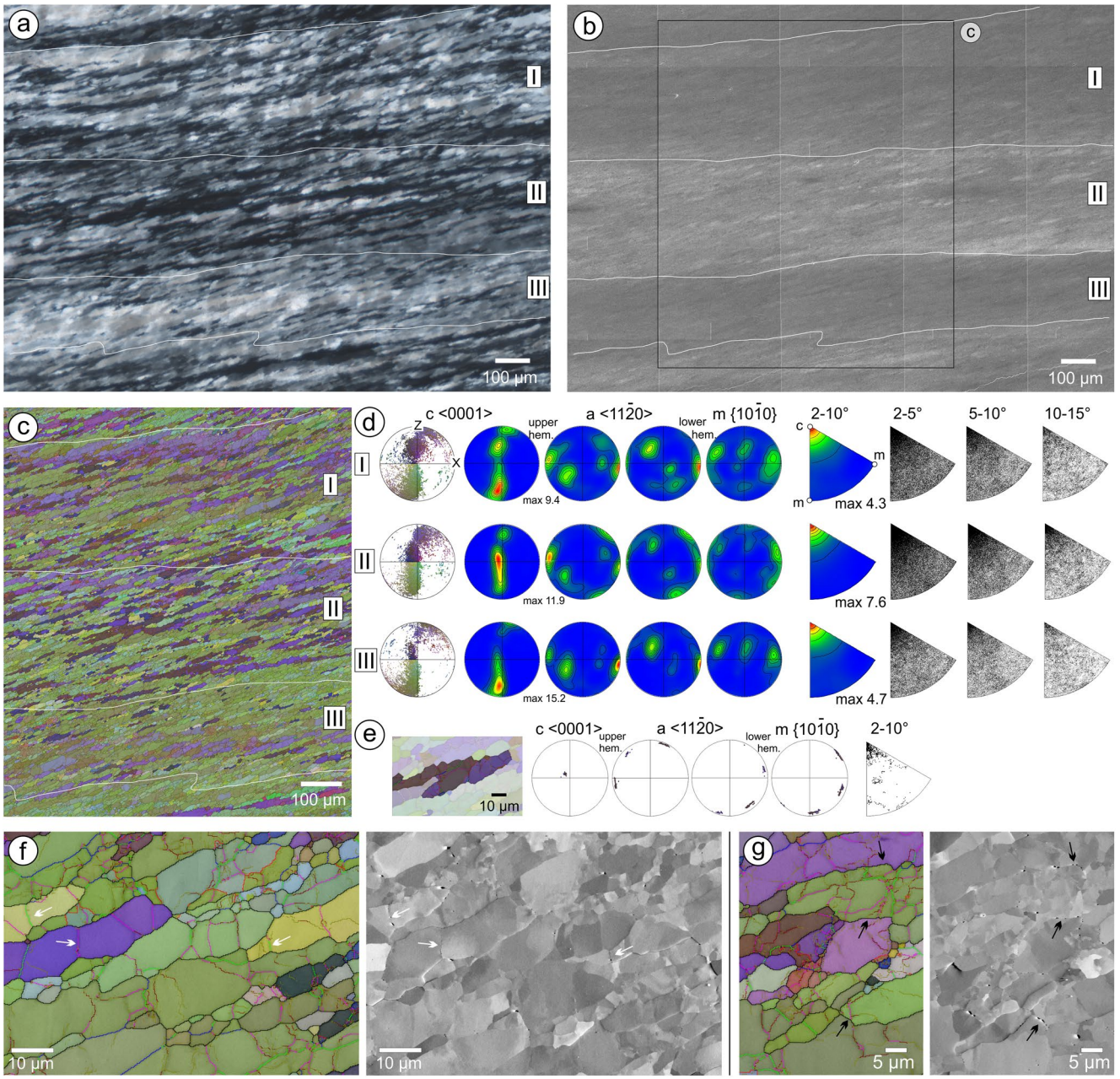

Figure 9. (Ultra)mylonite microstructure (sample HS-H2-2). (a) Optical microstructure (XPL). (b) SEM-CL image of same area as (a). (c) EBSD map (step size 200 nm) of area as marked in (b) color-coded with respect to Euler angles. White lines in (a–c) marks CL banding. Note in (a and c), elongated qtz_{2A} grains (aspect ratio up 10:1) are highly substructured and show an oblique shape preferred orientation (SPO). (d) Orientation data of different CL-bands (I-III) are presented as pole figures and misorientation axis of LAB (2–15°) as inverse pole figures. Note, the main cluster around <*c*> indicates prism<*a*> slip (Neumann, 2000). Density maxima (*mrd*) are given. (e) Elongated substructured grain shows a dispersion path around <*c*> and a clustering of LAB misorientation axis in inverse pole figures also around <*c*>. (f, g) Microstructure of elongated and highly substructured quartz grains. EBSD maps (left) and corresponding OC images (right). Subgrain size is in the same order as the new small grains; 1–10 µm. White arrows in (f) indicate LAB; black arrows indicate HAB in (g), decorated with pores. Boundary levels in EBSD maps follows key of Figure 5.

The SIMS data reveals very homogenous low [Ti] (0.3–0.6 ppm) for the dark CL layers (Figure 11a). The CL-brighter (ultra)mylonitic layers are more heterogeneous in the [Ti] (0.8–2.2 ppm) as reflected in the heterogeneous CL shade. Many of the elongated recrystallized grains (qtz_{2A}) show CL-brighter cores and CL-darker structures along the HAB (especially where GB pores are evident). In general, the CL shade can vary within and between these layers.

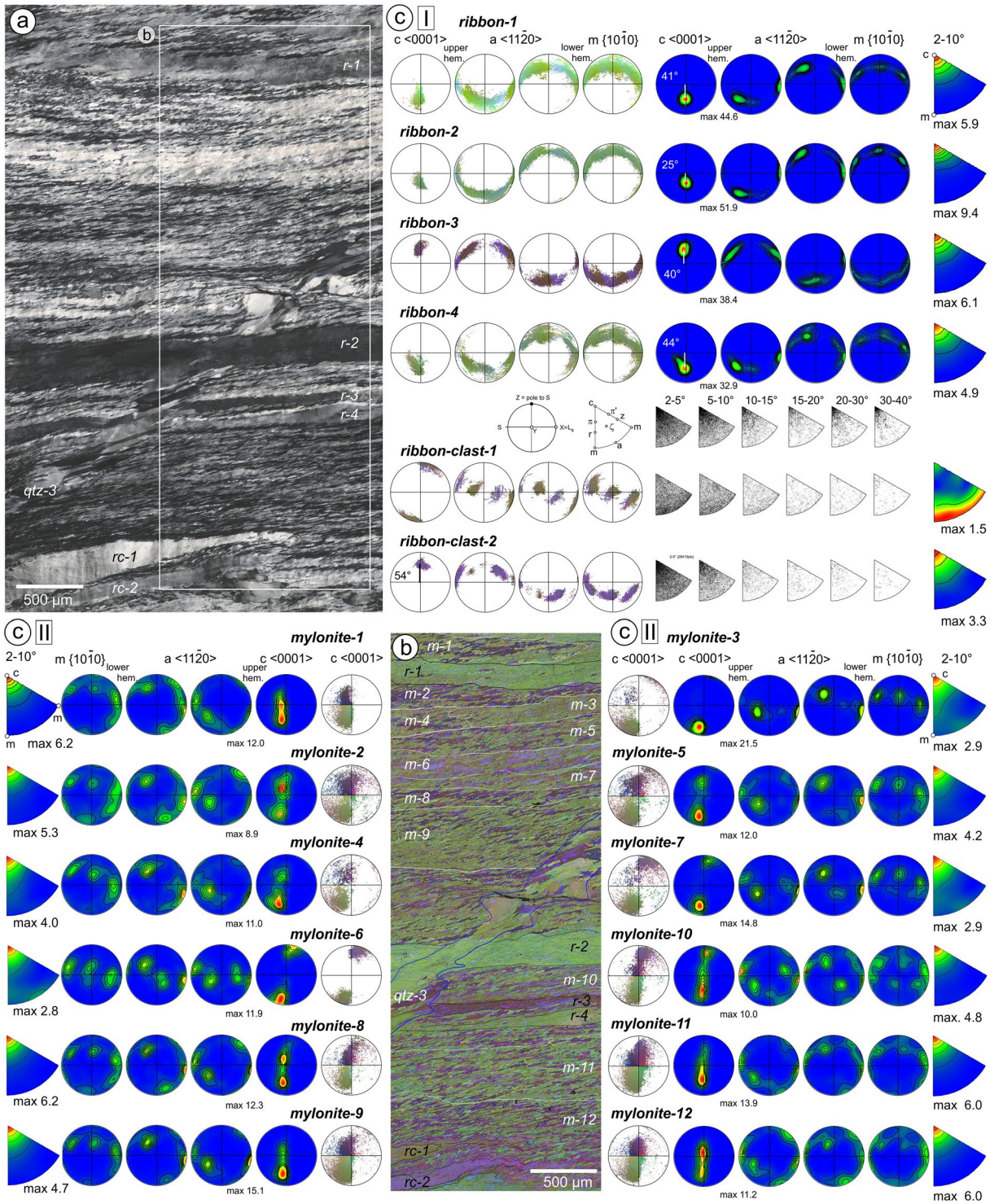

Figure 10. CPO of quartz ribbon grains (*r*) and (ultra)mylonitic layers (*m*) in high strain part of quartz vein. At the margin of the vein (lower part) ribbon-clasts (*rc*) are developed. (a) Optical microphotograph (XPL). (b) EBSD map color-coded with respect to Euler angles. Area is given in (a). White/black lines marks CL layering and blue lines mark the boundary between qtz_3 vein and (ultra)mylonitic fabric based on CL image (Figure 11a). (c) Orientation data of (I) quartz ribbons, ribbon-clasts and (II) (ultra)mylonite layers plotted as pole figures (PF) and misorientation axes as inverse pole figures (IPF). Maxima of contoured PF and IPF area given (*mrd*). In contoured *c*-axis plots of ribbons and the *c*-axis data plot of *ribbon-clast-2* the angle between the maximum and the center of the pole figures (*Y*-axis) is given. For ribbon-clasts and exemplary for *ribbon-4*, misorientation axes are plotted for specific misorientation angle intervals up to 40°. Note, for *ribbon-4* the axes persistently clusters around <*c*> for the entire range of misorientation angle (2–40°). This indicates that even high angle boundaries (>10–15°) are controlled by mainly prism<*a*> slip.

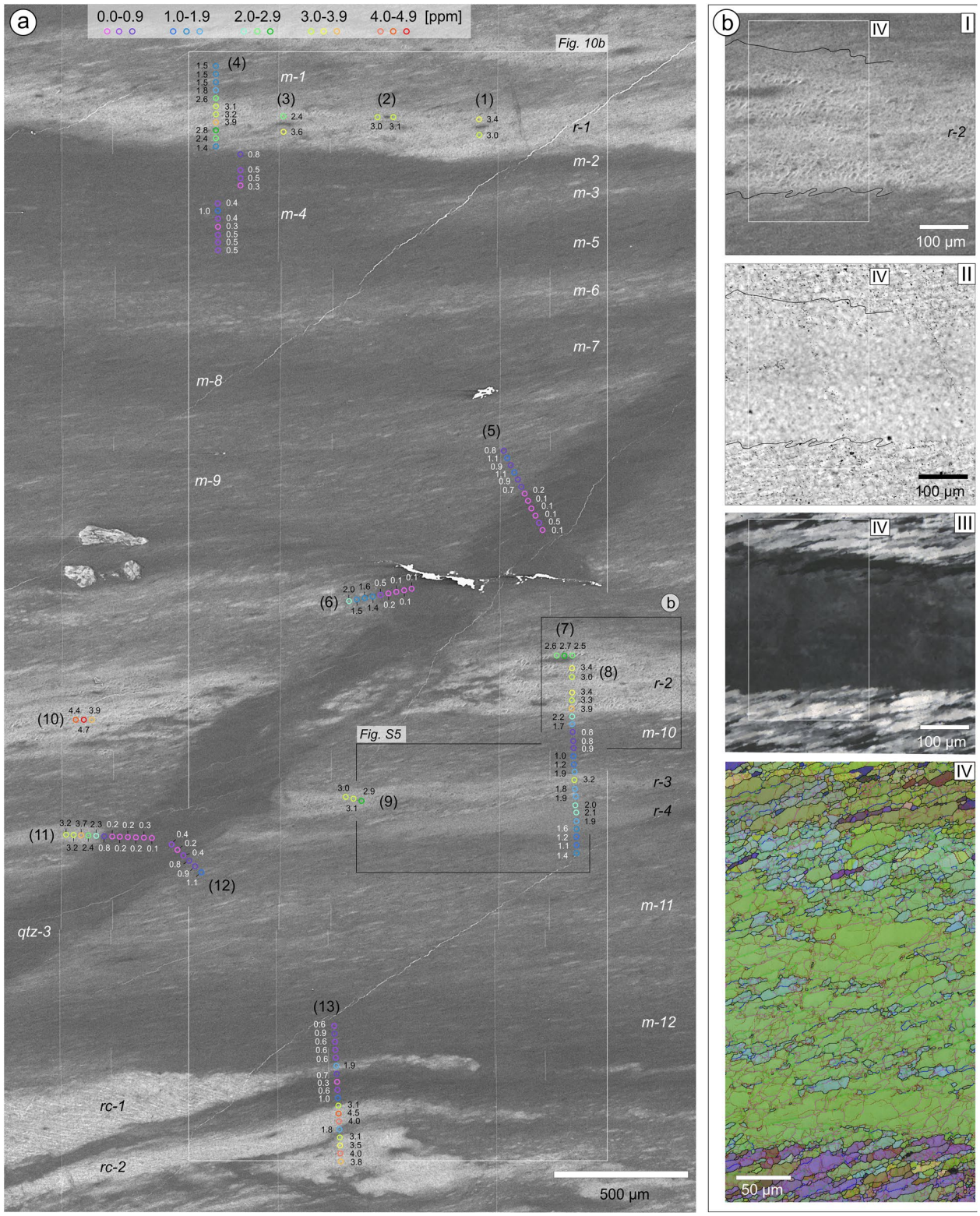

Figure 11. (a) SEM-CL image of (ultra)mylonite microstructure including (ultra)mylonitic layers (*m*), ribbon grains (*r*), ribbon-clasts (*rc*) and crosscutting late-stage quartz (qtz_3) vein. SIMS analysis spots are color-coded with respect to [Ti] – key is given. (b) (I-III) Enlargement of an area of *ribbon-2* (*r-2*) as marked in (a). Black lines in (I, II) represent upper and lower GB of *ribbon-2*. (I) SEM-CL image. (II, III) Optical microphotograph (PPL, XPL). In (II) *ribbon-2* shows low spatial density of fluid-related GB pores compared to the adjacent (ultra)mylonitic layers, corresponding to CL intensity variation in (a). (IV) EBSD map (step size: 500 nm) of area as marked in (I-III) color coded with respect to Euler angles. Boundary levels follow those of Figure 5. Note high spatial density of subgrain boundary in quartz ribbons.

4.3. Late-Stage Quartz (qtz_3) Veins

Late-stage quartz (qtz_3) veins (locally associated with chlorite) crosscut the foliation of the deformed quartz veins. These veins are easily identified in CL images by their dark, homogeneous shade crosscutting the CL banding of the protomylonitic to (ultra)mylonitic microstructure (Figures 11a, 12b–12d and 12f). Thin qtz_3 veins can be

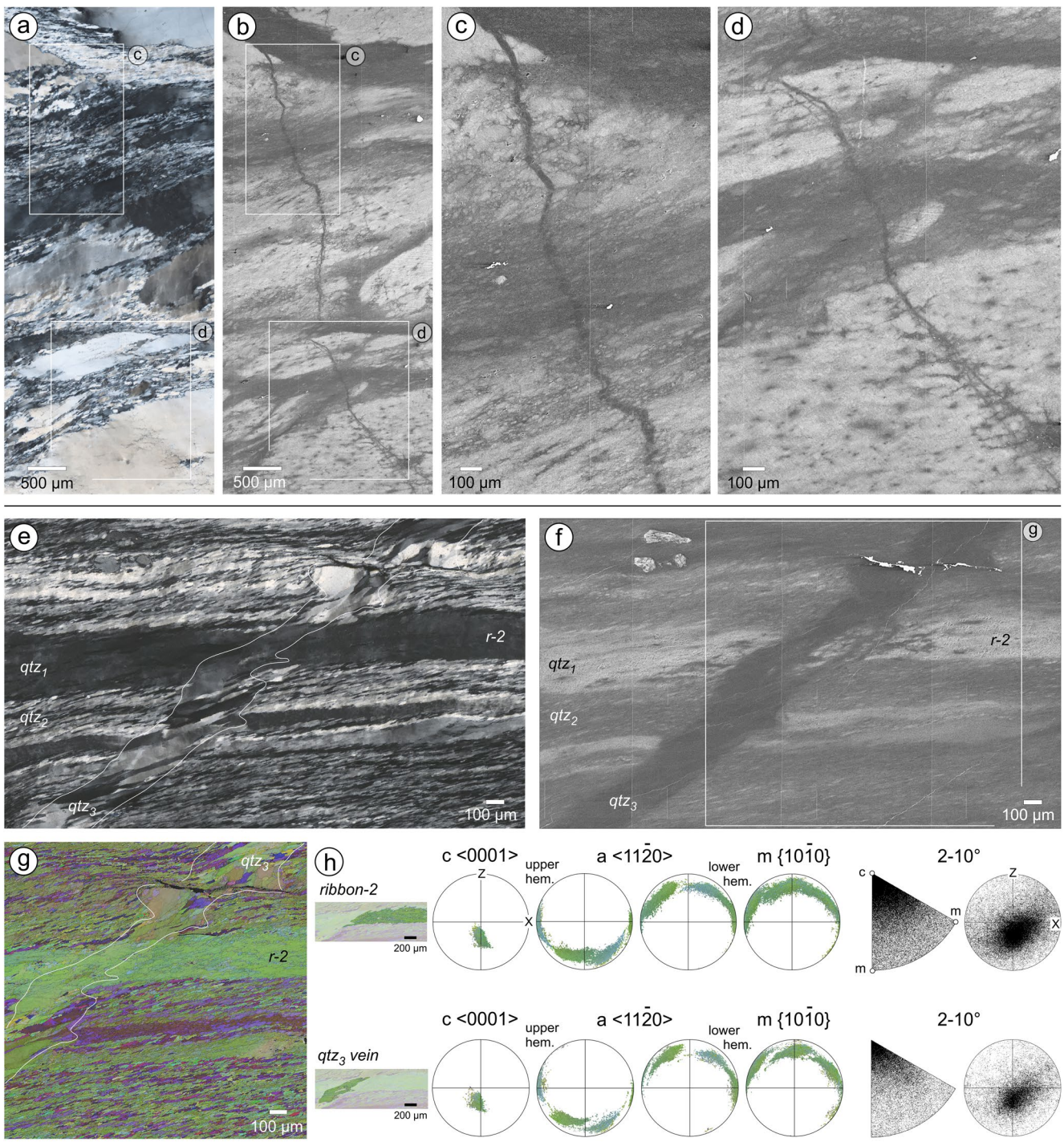

Figure 12. Late-stage quartz (qtz_3) veins crosscutting the protomylonitic (a–d) and (ultra)mylonitic (e–h) microstructure. Optical microphotographs (XPL; a, e) and corresponding SEM-CL images (b–d, f). (e–h) Qtz_3 veins crosscutting the (ultra)mylonite are syn-kinematically deformed. (g) EBSD map (step size: 500 nm) of area as marked in (f). White lines in (e) and (g) mark boundaries of qtz_3 vein. (h) Orientation data of *ribbon-2* and qtz_3 vein are plotted as pole figures (PF) and misorientation axes of LAB as inverse pole figures (IPF) and PF.

easily overlooked under the optical microscope due to the epitaxial growth of the quartz infilling on the host-vein quartz (Figure 12a). These veins are slightly involved in ductile deformation and show the same type of deformation features as the hosting deformed quartz and therefore are referred to as a syn-kinematic late stage quartz (see also Menegon & Fagereng, 2021). In Figure 12f the host ribbon grain (*r-2*) and the filling of the crosscutting qtz_3 vein show (a) the same dispersion patterns of the CPO in the pole figures, and (b) similar clustering around <*c*> and around the *Y*-axis in the misorientation axis plots in crystal and sample coordinates, respectively. Only minor dynamic recrystallization is recorded in the qtz_3 veins as result of the low accumulated strain. The homogeneous, dark CL shade corresponds to [Ti] in the range of 0.1–0.5 ppm (mainly 0.1–0.3 ppm) (*SIMS-profile 5*, *6*, *11* and *12* in Figure 11a).

4.4. Chlorite Thermometry

We applied chlorite thermometry (Bourdelle, 2021) to obtain independent information on the deformation temperature to complement the Ti-in-quartz estimates. This method has been shown to be particularly efficient for determining deformation temperature in the greenschist facies (Calzolari et al., 2018; Cantarero et al., 2014; Lacroix et al., 2012; Mizera et al., 2020; Zihlmann et al., 2018). We used the calibration of Vidal et al. (2005, 2006), which is based on two independent internal equilibria amongst the end members of the chlorite solid solution in presence of quartz and H_2O (see Ganne et al., 2012 for calculation details).

From three different microstructural sites in three samples (Figure S6 in Supporting Information S1) syn- and late-mylonitic chlorites were analyzed with an electron probe microanalyzer (see methodical section in Supporting Information S1). The equilibrium temperature was calculated for each analysis, assuming a pressure of 0.3 GPa (Table 1, see Section 5.3.2.2. for explanation). Syn-kinematic chlorite from microshear zones and strain shadows (Figure S6a in Supporting Information S1) yields temperatures between 238 and 268°C. Chlorite growing in garnet cracks is interpreted as syn-to late-kinematic (Figure S6b in Supporting Information S1) and yielded temperatures in the range between 272 and 352°C. The unoriented chlorite from a syn-deformational qtz_3 vein crosscutting the mylonitic foliation (Figure S6c in Supporting Information S1, see Section 4.3) yields temperatures between 265 and 333°C.

The estimated temperatures are affected by an error of 30°C (Plunder et al., 2012) to 50°C (Powell & Holland, 2008). Increasing the ambient pressure to 0.5 GPa results in an increase of the sample average temperature of less than 10°C. A high degree of oxidation tends to yield a low temperature (Vidal et al., 2005, 2006). Therefore, the largest source of error is likely to be the unknown ferrous/ferric iron ratio of each chlorite analysis. However, tests carried out by varying the range of ferrous/ferric iron indicates that its impact remains within 50°C. With an uncertainty of 50°C, the average temperatures in the three microstructural sites overlap within error, implying that syn- and late-kinematic chlorite grew at similar conditions. Only one sample yielded temperature consistently below 300°C (Table 1). Owing to the irregular surface of chlorite in microshear zones and strain shadows in this sample (Figure S6aIII in Supporting Information S1) and the small number of analyses, less weight should be put on this sample. We therefore conclude that chlorite thermometry provides a reasonable estimate of 300 ± 50°C for the deformation temperature, most likely in the upper part of this range.

Table 1
Results of Chlorite Thermometry Showing the Number of Analyses, the Calculated Temperature Range, Average and Standard Deviation for Each Microstructural Site of Figure S6 in Supporting Information S1

Microstructural site	n	T min [°C]	T max [°C]	avg T [°C]	std T [°C]
A: *Chl* in strain shadow or microshear zone	13	238	268	255	11
B: *Chl* in garnet cracks, retrogression product of garnet	31	272	352	315	24
C: *Chl* in qtz_3 vein	38	265	333	300	19

5. Discussion

5.1. Conditions of Quartz Vein Formation and Deformation

The high temperature grain boundary migration microstructure (>500°C; e.g., Stipp et al., 2002) of the coarse-grained quartz veins (Figure 3), and its structural position, points to crystallization condition syn-kinematically to the main foliation evolution during amphibolite-facies conditions at 510–590°C and 0.5–0.6 GPa (Linner, 1999). The quartz veins were later exploited as ductile shear zones along a sub-vertical ca. W-E-striking pseudotachylyte-bearing fault/shear zone, with dextral strike-slip kinematics, cutting discordantly the main foliation of the host rocks. A strike-slip kinematic, and the association with pseudotachylytes, is typical of the Oligocene-Miocene faulting in the Austroalpine and Penninic units of the Eastern Alps (Ceccato & Pennacchioni, 2018; Mancktelow et al., 2001). These strike-slip faults accommodated shortening and the lateral escape of the Alpine stack at the front of the Dolomites indenter (Ratschbacher et al., 1989). Since only dextral shear sense is recorded in the mylonites and the brittle fault rocks, the shear zone most likely belongs to the dextral Periadriatic fault system active after 30 Ma (Mancktelow et al., 2001). This postdates the Cretaceous/Paleocene exhumation constrained by biotite Rb/Sr ages (Linner, 1999) and indicates that deformation took place at the base of the upper crust, consistent with (i) the temperatures estimated from the chlorite thermometry, and (ii) the occurrence of ultra-cataclasites and pseudotachylytes coeval with ductile shearing in the quartz veins.

5.2. Resetting of [Ti] During Deformation

Resetting the initial 3–4 ppm [Ti] of coarse-grained qtz_1 grains down to 0.3–0.5 ppm of recrystallized qtz_2 grains in strongly deformed domains is heterogeneous. Two main factors apparently caused resetting of the [Ti]: (a) the amount of free available fluids in combination with dynamic recrystallization is responsible for the strongest resetting, and (b) the development of SGB is responsible for a minor resetting. The SIMS analyses have established the strong correlation between the CL shade and [Ti]. In the following we use the term resetting to indicate the decrease of the [Ti] with respect to that of pristine vein quartz crystals, corresponding to change to darker CL gray shades. We discuss the influence of different parameters (fluids, recrystallization, CPO, clast orientation and strain) on the [Ti]/CL resetting.

5.2.1. Effect of Fluids

Syn-kinematic infiltration and/or re-distribution of free aqueous fluids (e.g., released from fluid inclusions of the protolithic quartz vein grains during deformation) played a major role in [Ti] resetting. We have no evidence that these fluids moved out of the quartz vein system during deformation. The main mechanism producing grain-scale fluid pathways is SGR recrystallization resulting in a pervasive network of fluid-permeable GB. As a result, there is a general switch to dark CL shades and low [Ti] from qtz_1 coarse grains to qtz_2 recrystallized aggregates (e.g., Figures 8f–8h). GB permeability is witnessed by widespread occurrence of pores along HAB, as reported in other quartz mylonites (Fitz Gerald et al., 2006). In contrast, LAB are either free of porosity or show only minor porosity (e.g., Figure 5i–5k and 7). The syn-kinematic fluid infiltration is well documented in Figure 6a, where there is a distinct degree of [Ti] resetting, in the recrystallized quartz matrix surrounding the composite quartz porphyroclast, between the low pressure domains (preferential sink of fluids, stronger resetting) and the high pressure domains (weaker resetting) (see schematic stress field, marked in Figure 6a). The contrast in CL shade between extensional and contractional sites is not associated with a change of CPO of the qtz_2 aggregate or of the active slip systems (Figures 6a–6c). [Ti] resetting along GB commonly affects a thickness by as much as several tens of microns (Figure 6a, Figure S4 in Supporting Information S1). An enhanced resetting may result from a combination of dissolution and precipitation along GB (Yund & Tullis, 1991). Especially in dilation sites a resetting by precipitation is very likely (e.g., Figure 4S) even when it cannot be unambiguously shown. Complete resetting is also evident even where the degree of recrystallization and the strain are low (e.g., tip of recrystallization zone in Figures 8f–8h) or is strictly localized along interconnected intracrystalline HAB (black arrows in Figures 8f–8h). On the other hand, in high strain zones at the shortening quarters around clasts the GB fluid was drained and moved to extensional and dilatant zones under microscale pressure gradients (Figure 6a). Therefore, in shortening quarters resetting took place to a minor extent despite the pervasive dynamic recrystallization (see also Section 5.2.1.2). Within strongly localized and recrystallized microstructures, for example, interconnected microshear zone network in the protomylonites (black arrows in Figures 4a–4d, Figure 5a and 5b, Figure S3 in Supporting Information S1) or between clasts in the (ultra)mylonites (white arrows in Figures 4c and 4d, black

arrows in Figures 4g and 4h), available fluids were concentrated and promoted a strong resetting (Figure S3 in Supporting Information S1).

A CL shade gradient toward the grain interior is observed along GB and locally along SGB (e.g., Figure 5e). Cherniak et al. (2007) showed that diffusion distances are limited at low temperatures. Ti volume diffusion over a distance of 1 µm is estimated to take more than 1 Ma at ~300°C (the inferred deformation temperature of the investigated quartz veins). This diffusion rate is too sluggish to explain the observed 3-10 µm-thick [Ti] zonation. However, dislocations can act as fast diffusion pathways in a process known as pipe diffusion (Legros et al., 2008). Most diffusion experiments have been carried out under static conditions and therefore probably underestimate diffusion rates of deformation microstructures (Chakraborty, 2008, and references within). In deformation experiments, Yund et al. (1981) concluded, based on dislocation density gradients, that pipe diffusion enhanced the diffusion coefficient for oxygen and therefore promoted faster chemical exchange in albite. Piazolo et al. (2016) showed direct evidence by atom probe tomography that trace elements within deformed zircons are concentrated along dislocations piled up at SGB. For the quartz veins studied here, [Ti] are too low to carry out atom probe analysis. However, CL gradients are mainly occur where GB and SGB are correlated with a high density of fluid-related pores, implying that diffusion is promoted by the presence of fluids in. Nachlas et al. (2018) speculated that enhanced diffusion along dislocation structures (pipe diffusion) may also contribute to [Ti] resetting.

5.2.1.1. Effect of Subgrain Boundaries

Resetting related to SGB ranges from (a) a strongly localized effect along individual SGB to (b) a nearly homogeneous effect in strongly substructured (high spatial density of SGB) domains. In both cases, associated GB pores are basically absent, and the degree of resetting is minor compared to wetted GB and SGB.

(i) Local [Ti] resetting along SGB

In Figure 5e the network of thin dark-gray CL linear features within the qtz_1 grain correspond to a LAB network (Figures 5f and 5k). Dislocations along SGB can cause non-bridging oxygen hole center defects under electron irradiation and act as intrinsic defects producing a 650 nm emission peak in the red wavelength range in quartz (Hamers et al., 2017 and references within). However, the CL network described above is not visible using a red filter (600–700 nm) or as brighter structures in the polychromatic CL images (as e.g., seen in Figure 11b-I). This observation excludes intrinsic defects being responsible for the observed CL features. We suggest that diffusion along SGB caused decreasing [Ti] (see Section 5.3). Note that the very localized CL shade darkening along SGB is too small for SIMS analysis (beam spot size ca. 10 × 15 µm, see methodical section in Supporting Information S1). Nachlas et al. (2018) experimentally simulated prograde deformation conditions by deforming Ti-undersaturated coarse-grained quartz clasts in a fine-grained Ti-saturated quartz matrix. They observed slightly brighter CL shades along SGB and to some extent also broader diffusion pattern from the SGB into the host grains. It was concluded that a higher [Ti] concentration occurred along SGB by diffusion.

(ii) Homogeneous [Ti] resetting in areas with high SGB density

The margin of deformed qtz_1 porphyroclasts commonly shows a gradual darkening of the CL shade toward the adjacent, CL-dark qtz_2 mylonitic matrix. This effect is especially marked where a high spatial density of SGB is present at the clast margin (Figures 6f–6i). The corresponding partial [Ti] resetting (up to 50 µm, *SIMS-profile 13* in Figures 6a and 6f) cannot result from sluggish volume diffusion of Ti (see above and Section 5.2.1.). Rather syn-kinematic rearrangement of SGB and migration within the relatively highly strained grain margins can explain the process of resetting. SGB migration was observed in metals, analogue materials (Drury et al., 1985; Urai et al., 1986) and in rock-salt (Bestmann et al., 2005). Nachlas et al. (2018) argued that SGB migration is able to reset the deformed parts of the grain, where SGR recrystallization is evident, to a uniform higher [Ti] compared to the host.

5.2.1.2. Effect of Clast Orientation, Strain, Recrystallization, and Available Fluid in Strongly Deformed Vein Portions

Highly strained quartz ribbons with high SGB spatial density and misorientation axes around <*c*> preserve the pristine CL/Ti signal (e.g., *ribbon-2*, Figures 10 and 11). This was also observed in the experiments of Nachlas et al. (2018). Therefore, continuous SGB rearrangement by mainly prism<*a*> slip, not leading to dynamic

recrystallization, allows homogeneous crystal deformation without resetting. Only marginal resetting took place within the quartz ribbons, which are nearly free of GB pores that act as barriers for fluids. However, at incipiently recrystallized ribbon tips, a higher spatial density of GB pores is evident and is associated with stronger resetting.

In the ultramylonite with the characteristic extinction banding there is no strict correlation between [Ti]/CL and the CPO (LAB misorientation axis and related slip systems), the density of GB pores or the (sub)grain size (Figures 10 and 11). However, the original orientation of the vein crystals plays a major role for the microstructural evolution during increasing deformation (Ceccato et al., 2017). The degree of the [Ti] resetting depends strongly on the amount of the available fluids, and only to a minor degree on the "cycles" of dynamic recrystallization (Takaki et al., 2009). A strong [Ti]/CL resetting occurs where fluids were (a) channeled in microshear zones (e.g., Figure 4c, 4d, 4g and 4h as marked by arrows; Figure S3 in Supporting Information S1), (b) concentrated in extensional quarters (strain shadows) around porphyroclasts (e.g., inset in Figures 4b and 6a) and (c) concentrated in dilatant sites of boudinage-like structures (e.g., Figure 6 and Figure S4 in Supporting Information S1, see also Bestmann & Pennacchioni, 2015). Figures 4c and 4d shows an example (marked by white arrows) where the dark CL shade indicates [Ti] resetting due to fluids directed preferentially into strain shadows and channeled in microshear zones between the array of clasts aligned in one layer in the mylonitic matrix. Comparable strain/recrystallization microstructures with lower fluid/rock volume ratio show minor [Ti] resetting (e.g., shortening quarters around porphyroclasts, Figure 6a) than the ones with a high fluid/rock volume ratio (Bestmann & Pennacchioni, 2015). Thus, the moderate and incomplete resetting took place under relative dry conditions due to continuous rearrangement and movement of SGB and GB during ongoing cycles of SGR recrystallization. This observation is supported by Ashley et al. (2014) and Bestmann and Pennacchioni (2015) who previously suggested the importance of an inter-crystalline fluid to promote Ti-removal from quartz during deformation by SGR recrystallization.

In summary, under conditions where SGR recrystallization and prism <*a*> intracrystalline slip are predominant, deformation-induced resetting of [Ti] in the deformed quartz veins remains heterogeneous up to high strain and pervasive recrystallization. The different crystallographic orientation of the vein crystals determines whether quartz persists as relatively low-strain porphyroclasts, stretches into mono-crystalline ribbons, or recrystallizes to mylonitic aggregates. Dynamic recrystallization by SGR represents an efficient process to dramatically increase the GB surface area per unit volume and importantly lead to an invasive permeability network, allowing fluids to reach grain interiors and therefore decreasing the diffusion length for compositional exchange. In fact, HAB commonly host GB fluids. Therefore recrystallization enhances permeability and fluid-assisted [Ti] re-equilibration. Microscale strain heterogeneities also result in pressure gradients that guide fluid redistribution and differential [Ti] re-equilibration between fluid-rich and fluid-poor domains even in fully recrystallized aggregates. We suggest that fluids are the main agent of [Ti] re-equilibration. In contrast to HAB, LAB are in most cases impermeable to fluids and induce only subordinate [Ti] re-setting. Mylonites commonly show a CPO banding where recrystallized and strongly elongated grains qtz_{2a} containing a high SGB density are surrounded by small qtz_{2b} grains. This microstructure reflects the derivation from original crystals with different crystallographic orientation that control the selective activation of the main intracrystalline slip systems. This CPO banding is in part reflected in the [Ti] re-setting indicating that the CPO affects the strength and fluid redistribution with a dependence on the original orientation of the vein crystals, the amount of strain within each band, and the amount of fluid available.

5.2.2. Influence of Late-Stage Syn-deformational Quartz (qtz_3) Veins

The fluid infiltration associated with the formation of the late-stage qtz_3 veins does not have a significant effect on the [Ti]/CL signature of the crosscut host mylonitic fabric. The crosscutting new qtz_3 veins show a homogenous dark CL shade in sharp contact with the CL shade banding of the host quartz vein (qtz_1, qtz_2) except for a very limited, micron-scale diffusional transition in contact to the ultramylonite (Figure 12f). This indicates that fluid percolation along the quartz veins was only effective during synchronous mylonitization by crystal-plastic deformation and no later fluid infiltration contributed to CL/[Ti] resetting. The evolving grain-scale microstructure during flow (especially associated with new GB formation by SGB recrystallization) provided transient and mobile porosity allowing fluid transport. This is consistent with the observed partitioning of fluids along pressure gradients induced by flow perturbation around porphyroclasts (e.g., inset in Figure 4b; Figures 4a and 4d).

5.3. Application of TitaniQ

5.3.1. TitaniQ of Quartz Vein Formation

TitaniQ calibrations (Huang & Audétat, 2012 – HA12; Thomas et al., 2010 – TH10) are based on synthetic quartz grown from silica-saturated aqueous fluid in presence of rutile. Synchrotron analysis of veins studied here reveals the occurrence of rutile inclusions within both the coarse quartz vein crystals and the recrystallized microshear zones (Figure S2 in Supporting Information S1). This constrains TiO_2 activity to unity ($a_{TiO2} = 1$) (e.g., Thomas et al., 2010). Assuming the pressure estimates of Linner (1999), the TH10 of pristine [Ti] (3.0–4.7 ppm) preserved in deformed quartz clasts yields 388–410°C (0.5 GPa) and 405–427°C (0.6 GPa). HA12 results in approximately 100°C higher temperatures; 492–519°C and 507–534°C. Therefore, TH10 calculations are far below the temperature of amphibolite facies metamorphism (510–590°C, Linner, 1999) during which the quartz veins have crystallized.

5.3.2. TitaniQ of Quartz Vein Deformation

5.3.2.1. Influence of Deformation Processes and Related Microstructures for Ti-in-qtz Re-Equilibration

Several studies have shown that SGR recrystallization is inefficient to cause [Ti] re-equilibration (e.g., Ashley et al., 2013; Grujic et al., 2011). Grujic et al. (2011) concluded that only grain boundary migration (GBM) above ~540°C can cause complete [Ti] resetting. Nachlas et al. (2018) showed experimentally that SGB migration is able to promote [Ti] resetting. Haertel et al. (2013) inferred that during retrograde deformation, SGR together with fluid-mediated bulging recrystallization were capable of re-equilibrating [Ti] at 350–400°C. However, they concluded that SGR recrystallization alone was not capable of re-equilibrating [Ti] (Haertel et al., 2013). These studies infer that SGR recrystallization represents a structural rearrangement of the lattice coupled with grain size reduction, but does not involve SiO_2 transport and therefore is not efficient for [Ti] re-equilibration. Further, the duration (cycles) of dynamic recrystallization and the amount of strain were inferred to play an important role in [Ti] resetting (Ashley et al., 2014; Bestmann & Pennacchioni, 2015; Kidder et al., 2013; Nachlas & Hirth, 2015). In this view, ultramylonites (i.e., portion of nearly complete dynamic recrystallization) should represent the best candidates for applying TitaniQ. Here we show that the amount of free fluids percolating through the specific microstructure (especially along GB) is critical in controlling [Ti] resetting. A precise strain threshold is not essential, instead almost complete resetting occurs along wetted HAB and/or where dilatation sites provided sinks for fluids and syn-kinematic quartz precipitation (Bestmann & Pennacchioni, 2015; Haertel et al., 2013). In those microstructures the [Ti] (0.2–0.3 ppm) is in the same range as in (ultra)mylonitic layers (showing high density of GB pores) characterized by homogeneous low dark CL and corresponding homogeneous low [Ti] (0.3–0.6 ppm).

5.3.2.2. Application of TitaniQ to (Ultra)Mylonites

As discussed above (Section 5.1), it can be reasonably assumed that the studied veins were deformed near the base of the brittle-ductile transition of the crust, ~300–350°C that roughly occurs at 10–12 km depth (e.g., Hirth & Beeler, 2015), corresponding to ~0.3 GPa. Acosta et al. (2020) pointed out that HA12 was experimentally calibrated at lower pressure (0.1–1.0 GPa) than TH10 (0.5–2.0 GPa) and therefore should ideally be more suitable for the investigated quartz veins. At 0.3 GPa, the temperatures calculated with the 2 calibrations differs by ca. 70–100°C for a [Ti] range of 0.2–0.6 ppm and for an a_{TiO2} range of 0.1–1, with HA12 giving systematically higher temperatures. Provided the assumed ambient conditions of ~300–350°C are correct, temperature values in this range are obtained with HA12 with $a_{TiO2} = 1$ (320–369°C) or with TH10 with $a_{TiO2} = 0.2$ (305–355°C). If our multi-methodological microstructural analysis allows identification of proper sites of compositional re-equilibration for TitaniQ, the use of HA12 and TH10 calibrations need to have a rigorous constraint on the Ti activity for the application of the thermometer (and the choice of the appropriate calibration). Small rutile inclusions are present within the coarse quartz vein crystals as well as along the crosscutting microshear zone showing the same dark CL shades as the ultramylonitic samples analysed by SIMS (Figure S2g, h in Supporting Information S1). Further, during dynamic recrystallization rutile inclusions within qtz_1 grains are exposed into the qtz_2 matrix and are in contact with the GB fluid. Therefore, we infer that mylonitic deformation occurred under Ti-saturated conditions due to water-assisted rapid diffusion along the interconnected GB network (Bromiley & Hiscock, 2016; Farver & Yund, 1991; Nachlas et al., 2018; Thomas & Watson, 2014). In summary, the calculated temperature of 320–369°C using HA12 (as the low-pressure TitaniQ calibration) and $a_{TiO2} = 1$ represents the most reliable estimate for the mylonitization of the quartz veins. Therefore, the TitaniQ and the chlorite thermometry are well

within error of each other for syn-kinematic deformation. It should be emphasized that, if the partially re-equilibrated mylonitic matrix of the shortening quarters around porphyroclasts (Profile-10 & 15 of Figure 6: [Ti] 1.5–2.5 ppm) is used for TitaniQ thermometry, the calculated deformation temperature is 415–444°C (HA12 at 0.3 GPa, $a_{TiO2} = 1$) that is, significantly higher than for the extensional reset quarters.

6. Conclusions

The studied quartz veins indicate that deformation-induced Ti-in-quartz resetting toward lower concentrations is possible in the regime of subgrain rotation (SGR) recrystallization. Field constraints and chlorite thermometry suggest that quartz vein deformation occurred at low temperatures (≤350°C) in the ductile field near the base of the brittle crust. The microstructural complexity of the quartz mylonites requires a careful selection of the domains of most complete re-equilibration for applying TitaniQ. This is only possible through a detailed correlated analysis by optical and SEM (cathodoluminescence, CL; backscatter orientation contrast, BSE-OC; electron backscatter diffraction, EBSD) microscopy as a necessary pre-requisite to Ti measurement by secondary ion mass spectrometry (SIMS). The measured [Ti] in most complete re-equilibrated mylonitic domains (e.g., strain shadows or microshear zones) yield consistent TitaniQ temperatures for the condition close to the brittle-ductile transition and rutile-buffered Ti activity (320–369°C applying HA12 calibration at 0.3 GPa).

Conflict of Interest

The authors declare no conflicts of interest relevant to this study.

Acknowledgments
This work was funded by the Deutsche Forschungsgemeinschaft DFG (BE 2413/3-1). GP acknowledge funding from the University of Padova (BIRD175145/17). Access to the SEM-EBSD facilities was provided by the Department of Werkstoffwissenschaften WW1, FAU Erlangen-Nürnberg, Germany. The Oxford Instruments CMOS-Symmetry EBSD detector was funded by the DFG (JA 2718/3-1). Jay Thomas is thanked for providing the synthetic Ti-doped quartz standard (QTiP-38, Ti 380 ppm), Djordje Grujic for the natural standard (TN-06, 0.3 ppm) and Steven Kidder for the Herkimer "Diamond" used as a Ti blank. Cees-Jan De Hoog is thanked for conducting SIMS measurements and processing at the School of Geosciences of the University of Edinburgh. We acknowledge Holger Stünitz for discussion and providing access to the SEM-CL spectra facilities at the Department of Geosciences at the Arctic University of Norway (Tromsö), and Amicia Lee and Tom-Ivar Eilertsen for their assistance. Christoph E. Schrank and Nicholas W. Phillips are thanked for their contribution with respect to the synchrotron data set. Part of this research was undertaken on the XFM beamline at the Australian Synchrotron, part of ANSTO. Rene Romer is thanked for support during electron microprobe analysis (chlorite thermometry) and Friederike Urban and Raphael Njul for sample preparation. Alexis Plunder is thanked for the chlorite thermometry blind test. We are grateful for constructive reviews of Steve Kidder and Leif Tokle and the assessment of an anonymous associated editor of JGR-Solid Earth. Open access funding enabled and organized by Projekt DEAL.

Data Availability Statement

The EBSD, WDX, SIMS and Synchrotron X-ray Fluorescence data used in this study are publicly available at http://doi.org/10.5281/zenodo.4923150

References

Acosta, M. D., Watkins, J. M., Reed, M. H., Donovan, J. J., & De Palolo, D. J. (2020). Ti-in-quartz: Evaluating the role of kinetics in high temperature crystal growth experiments. *Geochimica et Cosmochimica Acta*, *281*, 149–167. https://doi.org/10.1016/j.gca.2020.04.030

Ashley, K. T., Carlson, W. D., Law, R. D., & Tracy, R. J. (2014). Ti resetting in quartz during dynamic recrystallization: Mechanisms and significance. *American Mineralogist*, *99*, 2025–2030. https://doi.org/10.2138/am-2014-4943

Ashley, K. T., Webb, L. E., Spear, F. S., & Thomas, J. B. (2013). P-T-D histories from quartz: A case study for the application of the TitaniQ thermobarometer to progressive fabric development in metapelites. *Geochemistry, Geophysics, Geosystems*, *14*, 3821–3843. https://doi.org/10.1002/ggge.20237

Behr, W. M., & Platt, J. P. (2011). A naturally constrained stress profile through the middle crust in an extensional terrane. *Earth and Planetary Science Letters*, *303*, 181–192. https://doi.org/10.1016/j.epsl.2010.11.044

Bell, T. H., & Hammond, R. L. (1984). On the internal geometry of mylonite zones. *The Journal of Geology*, *92*(6), 667–686. https://doi.org/10.1086/628905

Bestmann, M., & Pennacchioni, G. (2015). Ti distribution in quartz across a heterogeneous shear zone within a granodiorite: The effect of deformation mechanism and strain on Ti resetting. *Lithos*, *227*, 37–56. https://doi.org/10.1016/j.lithos.2015.03.009

Bestmann, M., Piazolo, S., Spiers, C. J., & Prior, D. J. (2005). Microstructural evolution during initial stages of static recovery and recrystallization: New insights from in-situ heating experiments combined with electron backscatter diffraction analysis. *Journal of Structural Geology*, *27*, 447–457. https://doi.org/10.1016/j.jsg.2004.10.006

Bourdelle, F. (2021). Low-Temperature Chlorite Geothermometry and Related Recent Analytical Advances: A Review. *Minerals*, *11*(2), 130. https://doi.org/10.3390/min11020130

Bromiley, G. D., & Hiscock, M. (2016). Grain boundary diffusion of titanium in polycrystalline quartz and its implications for titanium in quartz (TitaniQ) geothermobarometry. *Geochimica et Cosmochimica Acta*, *178*, 281–290. https://doi.org/10.1016/j.gca.2016.01.024

Calzolari, G., Rossetti, F., Ault, A. K., Lucci, F., Olivetti, V., & Nozaem, R. (2018). Hematite (U-Th)/He thermochronometry constrains intraplate strike-slip faulting on the Kuh-e-Faghan Fault, central Iran. *Tectonophysics*, *728*, 41–54. https://doi.org/10.1016/j.tecto.2018.01.023

Cantarero, I., Lanari, P., Vidal, O., Alías, G., Travé, A., & Baqués, V. (2014). Long-term fluid circulation in extensional faults in the central Catalan Coastal Ranges: P–T constraints from neoformed chlorite and K-white mica. *International Journal of Earth Sciences*, *103*(1), 165–188. https://doi.org/10.1007/s00531-013-0963-8

Ceccato, A., & Pennacchioni, G. (2018). Structural evolution of the Rieserferner pluton in the framework of the Oligo-Miocene tectonics of the eastern Alps. *Journal of Structural Geology*, *116*, 64–80. https://doi.org/10.1016/j.jsg.2018.08.004

Ceccato, A., Pennacchioni, G., Menegon, L., & Bestmann, M. (2017). Crystallographic control and texture inheritance during mylonitization of coarse grained quartz veins. *Lithos*, *290–291*, 210–227. https://doi.org/10.1016/j.lithos.2017.08.005

Chakraborty, S. (2008). Diffusion in solid silicates. *Annual Review of Earth and Planetary Sciences*, *36*, 153–190. https://doi.org/10.1146/annurev.earth.36.031207.124125

Cherniak, D. J., Watson, E. B., & Wark, D. A. (2007). Ti diffusion in quartz. *Chemical Geology*, *236*(1–2), 65–74. https://doi.org/10.1016/j.chemgeo.2006.09.001

Drury, M. R., Humphreys, F. J., & White, S. H. (1985). Large strain deformation studies using polycrystalline magnesium as a rock analogue. Part II: Dynamic recrystallization mechanisms at high temperatures. *Physics of the Earth and Planetary Interiors*, *40*, 208–222. https://doi.org/10.1016/0031-9201(85)90131-1

Farver, J. R., & Yund, R. A. (1991). Oxygen diffusion in quartz: Dependence on temperature and water fugacity. *Chemical Geology*, *90*(1–2), 55–70. https://doi.org/10.1016/0009-2541(91)90033-n

Fitz Gerald, J. D., Mancktelow, N. S., Pennaccioni, G., & Kunze, K. (2006). Ultrafine-grained quartz mylonites from high-grade shear zones: Evidence for strong dry middle to lower crust. *Geology*, *34*, 369–372. https://doi.org/10.1130/g22099.1

Ganne, J., De Andrade, V., Weinberg, R. F., Vidal, O., Dubacq, B., Kagambega, N., et al. (2012). Modern-style plate subduction preserved in the Palaeoproterozoic West African craton. *Nature Geoscience*, *5*(1), 60–65. https://doi.org/10.1038/ngeo1321

Grujic, D., Stipp, M., & Wooden, J. (2011). Thermometry of quartz mylonites: Importance of dynamic recrystallization on Ti-in-quartz re-equilibration. *Geochemistry, Geophysics, Geosystems*, *12*, Q06012. https://doi.org/10.1029/2010GC003368

Haertel, M., Herwegh, M., & Pettke, T. (2013). Titanium-in-quartz thermometry on synkinematic quartz veins in a retrograde crustal-scale normal fault zone. *Tectonophysics*, *608*, 468–481. https://doi.org/10.1016/j.tecto.2013.08.042

Hamers, M. F., Pennock, F. M., & Drury, M. R. (2017). Scanning electron microscope cathodoluminescence imaging of subgrain boundaries, twins and planar deformation features in quartz. *Physics and Chemistry of Minerals*, *44*, 263–275. https://doi.org/10.1007/s00269-016-0858-x

Hanmer, S., & Passchier, C. (1991). Shear sense indicators: A review. *Geological Survey of Canada Paper*, *90*, 1–71. https://doi.org/10.4095/132454

Hauke, M., Froitzheim, N., Nagel, T. J., Miladinova, I., Fassmer, K., Fonseca, R. O. C., et al. (2019). Two high-pressure metamorphic events, Variscan and Alpine, dated by Lu–Hf in an eclogite complex of the Austroalpine nappes (Schobergruppe, Austria). *International Journal of Earth Sciences*, *108*, 1317–1331. https://doi.org/10.1007/s00531-019-01708-8

Hirth, G., & Beeler, N. M. (2015). The role of fluid pressure on frictional behavior at the base of the seismogenic zone. *Geology*, *43*, 223–226. https://doi.org/10.1130/G36361.1

Hirth, G., & Tullis, J. (1992). Dislocation creep regimes in quartz aggregates. *Journal of Structural Geology*, *14*, 145–159. https://doi.org/10.1016/0191-8141(92)90053-y

Howard, D. L., de Jonge, M. D., Afshar, N., Ryan, C. G., Kirkham, R., Reinhardt, J., et al. (2020). The XFM beamline at the Australian Synchrotron. *Journal of Synchrotron Radiation*, *27*, 1447–1458. https://doi.org/10.1107/S1600577520010152

Huang, R., & Audétat, A. (2012). The titanium-in-quartz (TitaniQ) thermobarometer: A critical examination and re-calibration. *Geochimica et Cosmochimica Acta*, *84*, 75–89. https://doi.org/10.1016/j.gca.2012.01.009

Kidder, S., Avouac, J.-P., & Chand, Y.-C. (2013). Application of titanium-in-quartz thermobarometry to greenschistfacies veins and recrystallized quartzites in the Hsüehshan range, Taiwan. *Journal of Geophysical Research: Solid Earth*, *4*, 1–21. https://doi.org/10.5194/se-4-1-2013

Kidder, S., Toy, V., Prior, D., Little, T., & MacRae, C. (2018). Constraints on alpine fault (New Zealand) mylonitization temperatures and geothermal gradient from Ti-in-quartz thermobarometry. *Journal of Geophysical Research: Solid Earth*, *9*, 1123–1139. https://doi.org/10.5194/se-9-1123-2018

Kohn, M. J., & Northrup, C. J. (2009). Taking mylonites' temperatures. *Geology*, *37*, 47–50. https://doi.org/10.1130/g25081a.1

Korchinski, M., Little, T. A., Smith, E., & Millet, M.-A. (2012). Variation of Ti-in-quartz in gneiss domes exposing the world's youngest ultrahigh-pressure rocks, D'Entrecasteaux Islands, Papua New Guinea. *Geochemistry, Geophysics, Geosystems*, *13*, Q0AL01. https://doi.org/10.1029/2012GC004230

Krenn, E., Schulz, B., & Finger, F. (2012). Three generations of monazite in Austroalpine basement rocks to the south of the Tauern Window: Evidence for Variscan, Permian and Eo-Alpine metamorphic events. *Swiss Journal of Geosciences*, *105*(3), 343–360. https://doi.org/10.1007/s00015-012-0104-6

Lacroix, B., Charpentier, D., Buatier, M., Vennemann, T., Labaume, P., Adatte, T., et al. (2012). Formation of chlorite during thrust fault reactivation. Record of fluid origin and P–T conditions in the Monte Perdido thrust fault (southern Pyrenees). *Contributions to Mineralogy and Petrology*, *163*(6), 1083–1102. https://doi.org/10.1007/s00410-011-0718-0

Legros, M., Dehm, G., Arzt, E., & Balk, T. J. (2008). Observation of giant diffusivity along dislocation cores. *Science*, *319*, 1646–1649. https://doi.org/10.1126/science.1151771

Linner, M. (1999). *Entwicklung der Eklogite im Schoberkristallin als Beleg für frühalpidische kontinentale Subduktion im Ostalpinen Kristallin* (p. 211). Thesis, University of Vienna.

Mancktelow, N. S., & Pennacchioni, G. (2004). The influence of grain boundary fluids on the microstructure of quartz-feldspar mylonites. *Journal of Structural Geology*, *26*, 47–69. https://doi.org/10.1016/s0191-8141(03)00081-6

Mancktelow, N. S., Stöckli, D. F., Grollimund, B., Müller, W., Fügenschuh, B., Viola, G., et al. (2001). The DAV and Periadriatic fault systems in the Eastern Alps south of the Tauern window. *International Journal of Earth Sciences*, *90*(3), 593–622. https://doi.org/10.1007/s005310000190

Menegon, L., & Fagereng, Å. (2021). Tectonic pressure gradients during viscous creep drive fluid flow and brittle failure at the base of the seismogenic zone. *Geology*, *49*, 1255–1259. https://doi.org/10.1130/G49012.1

Mizera, M., Little, T., Boulton, C., Prior, D., Watson, E., Biemiller, J., & Shigematsu, N. (2020). Slow-to-fast deformation in mafic fault rocks on an active low-angle normal fault, Woodlark Rift, SE Papua New Guinea. *Geochemistry, Geophysics, Geosystems*, *21*(11), e2020GC009171. https://doi.org/10.1029/2020gc009171

Nachlas, W. O., & Hirth, G. (2015). Experimental constraints on the role of dynamic recrystallization on resetting the Ti-in-quartz thermobarometer. *Journal of Geophysical Research: Solid Earth*, *120*, 8120–8137. https://doi.org/10.1002/2015JB012274

Nachlas, W. O., Thomas, J. B., & Hirth, G. (2018). TitaniQ deformed: Experimental deformation of out-of-equilibrium quartz porphyroclasts. *Journal of Structural Geology*, *116*, 207–222. https://doi.org/10.1016/j.jsg.2018.07.012

Nachlas, W. O., Whitney, D. L., Teyssier, C., Bagley, B., & Mulch, A. (2014). Titanium concentration in quartz as a record of multiple deformation mechanisms in an extensional shear zone. *Geochemistry, Geophysics, Geosystems*, *15*, 1374–1397. https://doi.org/10.1002/2013GC005200

Negrini, M., Stünitz, H., Berger, A., & Morales, L. F. G. (2014). The effect of deformation on the TitaniQ geothermobarometer: An experimental study. *Contributions to Mineralogy and Petrology*, *167*, 982. https://doi.org/10.1007/s00410-014-0982-x

Neumann, B. (2000). Texture development of recrystallized quartz polycrystals unravelled by orientation and misorientation characteristics. *Journal of Structural Geology*, *22*, 1695–1711. https://doi.org/10.1016/s0191-8141(00)00060-2

Pennacchioni, G., & Mancktelow, N. S. (2018). Small-scale ductile shear zones: Neither extending, nor thickening, nor narrowing. *Earth-Science Reviews*, *184*, 1–12. https://doi.org/10.1016/j.earscirev.2018.06.004

Pennacchioni, G., Menegon, L., Leiss, B., Nestola, F., & Bromiley, G. (2010). Development of crystallographic preferred orientation and microstructure during plastic deformation of natural coarse-grained quartz veins. *Journal of Geophysical Research: Solid Earth*, *115*, B12405. https://doi.org/10.1029/2010jb007674

Piazolo, S., La Fontaine, A., Trimby, P., Harley, S., Yang, L., Armstrong, R., & Cairney, J. M. (2016). Deformation-induced trace element redistribution in zircon revealed using atom probe tomography. *Nature Communications*, *7*, 10490. https://doi.org/10.1038/ncomms10490

Plunder, A., Agard, P., Dubacq, B., Chopin, C., & Bellanger, M. (2012). How continuous and precise is the record of P–T paths? Insights from combined thermobarometry and thermodynamic modelling into subduction dynamics (Schistes Lustrés, W. Alps). *Journal of Metamorphic Geology*, *30*(3), 323–346. https://doi.org/10.1111/j.1525-1314.2011.00969.x

Powell, R., & Holland, T. J. B. (2008). On thermobarometry. *Journal of Metamorphic Geology*, *26*(2), 155–179. https://doi.org/10.1111/j.1525-1314.2007.00756.x

Ratschbacher, L., Frisch, W., Neubauer, F., Schmid, S. M., & Neugebauer, J. (1989). Extension in compressional orogenic belts: The Eastern Alps. *Geology*, *17*, 404–407. https://doi.org/10.1130/0091-7613(1989)017<0404:eicobt>2.3.co;2

Rosenberg, C. L., Brun, J. P., Cagnard, F., & Gapais, D. (2007). Oblique indentation in the Eastern Alps: Insights from laboratory experiments. *Tectonics*, *26*(2). https://doi.org/10.1029/2006tc001960

Schulz, B. (1993). Mineral chemistry, geothermobarometry and pre-Alpine high-pressure metamorphism of eclogitic amphibolites and mica schists from the Schobergruppe, Austroalpine basement, Eastern Alps. *Mineralogical Magazine*, *57*(387), 189–202. https://doi.org/10.1180/minmag.1993.057.387.01

Schuster, R., Daurer, A., Krenmayr, H.-G., Linner, M., Mandl, G. W., Pestal, G., & Reitner, J. M. (2014). *Rocky Austria: The Geology of Austria - brief and colourful* (pp. 1–80). Geological Survey Austria.

Spear, F. S., & Wark, D. (2009). Cathodoluminescence imaging and titanium thermometry in metamorphic quartz. *Journal of Metamorphic Geology*, *27*, 187–205. https://doi.org/10.1111/j.1525-1314.2009.00813.x

Stipp, M., Stünitz, H., Heilbronner, R., & Schmid, S. M. (2002). The Eastern Tonale fault zone: A "natural laboratory" for crystal plastic deformation of quartz over a temperature range from 250 to 700°C. *Journal of Structural Geology*, *24*, 1861–1884. https://doi.org/10.1016/s0191-8141(02)00035-4

Takaki, T., Hisakuni, Y., Hirouchi, T., Yamanaka, A., & Tomita, Y. (2009). Multi-phase-field simulations for dynamic recrystallization. *Computational Materials Science*, *45*(4), 881–888. https://doi.org/10.1016/j.commatsci.2008.12.009

Thomas, J. B., & Watson, E. B. (2014). Diffusion and partitioning of magnesium in quartz grain boundaries. *Contributions to Mineralogy and Petrology*, *168*, 1–12. https://doi.org/10.1007/s00410-014-1068-5

Thomas, J. B., Watson, E. B., Spear, F. S., Shemella, P. T., Nayak, S. K., & Lanzirozzi, A. (2010). TitaniQ under pressure: The effect of pressure and temperature on the solubility of Ti in quartz. *Contributions to Mineralogy and Petrology*, *160*, 743–759. https://doi.org/10.1007/s00410-010-0505-3

Trepmann, C., & Seybold, L. (2019). Deformation at low and high stress-loading rates. *Geoscience Frontiers. Geoscience Frintiers*, *10*, 43–54. https://doi.org/10.1016/j.gsf.2018.05.002

Urai, J. L., Means, W. D., & Lister, G. S. (1986). In B. E. Hobbs, & H. C. Heard (Eds.), *Dynamic recrystallization of minerals. Mineral and rock deformation: The Paterson volume* (pp. 1–49). American Geophysical Union.

Vidal, O., de Andrade, V., Lewin, E., Munoz, M., Parra, T., & Pascarelli, S. (2006). P–T-deformation-Fe3+/Fe2+ mapping at the thin section scale and comparison with XANES mapping: Application to a garnet-bearing metapelite from the Sambagawa metamorphic belt (Japan). *Journal of Metamorphic Geology*, *24*(7), 669–683. https://doi.org/10.1111/j.1525-1314.2006.00661.x

Vidal, O., Parra, T., & Vieillard, P. (2005). Thermodynamic properties of the Tschermak solid solution in Fe-chlorite: Application to natural examples and possible role of oxidation. *American Mineralogist*, *90*(2–3), 347–358. https://doi.org/10.2138/am.2005.1554

Wark, D. A., & Spear, F. S. (2005). Titanium in quartz: Cathodoluminescence and thermometry. *Geochimica et Cosmochimica Acta - Supplement*, *69*, A592.

Wark, D. A., & Watson, E. B. (2006). TitaniQ: A titanium-in-quartz geothermometer. *Contributions to Mineralogy and Petrology*, *152*, 743–754. https://doi.org/10.1007/s00410-006-0132-1

White, S. H. (1976). The effects of strain on the microstructure, fabrics, and deformation mechanisms in quartzites. *Philosophical Transactions of the Royal Society of London A*, *283*, 69–86.

Yund, R. A., Smith, B. M., & Tullis, J. (1981). Dislocation-assisted diffusion of oxygen in albite. *Physics and Chemistry of Minerals*, *7*, 185–189. https://doi.org/10.1007/bf00307264

Yund, R. A., & Tullis, J. (1991). Compositional changes of minerals associated with dynamic recrystallization. *Contributions to Mineralogy and Petrology*, *108*, 346–355. https://doi.org/10.1007/BF00285942

Zihlmann, B., Müller, S., Coggon, R. M., Koepke, J., Garbe-Schönberg, D., & Teagle, D. A. (2018). Hydrothermal fault zones in the lower oceanic crust: An example from Wadi Gideah, Samail ophiolite, Oman. *Lithos*, *323*, 103–124. https://doi.org/10.1016/j.lithos.2018.09.008

References From the Supporting Information

Bestmann, M., Pennacchioni, G., Frank, G., Göken, M., & de Wall, H. (2011). Pseudotachylyte in muscovite-bearing quartzite: Coseismic friction-induced melting and plastic deformation of quartz. *Journal of Structural Geology*, *33*, 169–186. https://doi.org/10.1016/j.jsg.2010.10.009

Bestmann, M., & Prior, D. J. (2003). Intragranular dynamic recrystallization in naturally deformed calcite marble: Diffusion accommodated grain boundary sliding as a result of subgrain rotation recrystallization. *Journal of Structural Geology*, *25*, 1597–1613. https://doi.org/10.1016/s0191-8141(03)00006-3

Ryan, C. G., & Jamieson, D. N. (1993). Dynamic analysis: On-line quantitative PIXE microanalysis and its use in overlap-resolved elemental mapping. *Nuclear Instruments & Methods in Physics Research, Section B*, *77*, 203–214. https://doi.org/10.1016/0168-583x(93)95545-g

Ryan, C. G., Kirkham, R., de Jonge, M. D., Siddons, D. P., van der Ent, A., Pagés, A., et al. (2018). The Maia Detector and Event Mode. *Synchrotron Radiation News*, *31*, 21–27. https://doi.org/10.1080/08940886.2018.1528430

Siddons, D. P., Kirkham, R., Ryan, C. G., De Geronimo, G., Dragone, A., Kuczewski, A. J., et al. (2014). Maia X-ray microprobe detector array system. *Journal of Physics: Conference Series*, *499*, 012001. https://doi.org/10.1088/1742-6596/499/1/012001